Monthly Notices
of the
ROYAL ASTRONOMICAL SOCIETY

MNRAS **434,** 3322–3336 (2013) doi:10.1093/mnras/stt1241
Advance Access publication 2013 August 2

The preferentially magnified active nucleus in IRAS F10214+4724 – III. VLBI observations of the radio core

R. P. Deane,[1,2⋆] S. Rawlings,[1] M. A. Garrett,[3,4] I. Heywood,[1] M. J. Jarvis,[1,5,6] H.-R. Klöckner,[1,7] P. J. Marshall[1] and J. P. McKean[3]

[1]*Astrophysics, Department of Physics, University of Oxford, Keble Road, Oxford OX1 3RH, UK*
[2]*Astrophysics, Cosmology and Gravity Centre, Department of Astronomy, University of Cape Town, Private Bag X3, Rondebosch 7701, South Africa*
[3]*ASTRON, The Netherlands Institute for Radio Astronomy, Postbus 2, NL-7990 AA Dwingeloo, the Netherlands*
[4]*Leiden Observatory, Leiden University, Postbus 9513, NL-2300 RA Leiden, the Netherlands*
[5]*Centre for Astrophysics Research, Science & Technology Research Institute, University of Hertfordshire, Hatfield AL10 9AB, UK*
[6]*Physics Department, University of the Western Cape, Cape Town 7535, South Africa*
[7]*Max-Planck-Institut für Radioastronomie, Auf dem Hügel 69, D-53121 Bonn, Germany*

Accepted 2013 July 6. Received 2013 July 4; in original form 2012 April 3

ABSTRACT

We report 1.7 GHz very long baseline interferometry (VLBI) observations of IRAS F10214+4724, a lensed $z = 2.3$ obscured quasar with prodigious star formation. We detect what we argue to be the obscured active nucleus with an effective angular resolution of <50 pc at $z = 2.3$. The $S_{1.7} = 210\,\mu$Jy (9σ) detection of this unresolved source is located within the *Hubble Space Telescope* rest-frame ultraviolet/optical arc, however, $\gtrsim$100 mas northwards of the arc centre of curvature. This leads to a source-plane inversion that places the European VLBI Network detection to within milliarcseconds of the modelled cusp caustic, resulting in a very large magnification ($\mu \sim 70$), over an order of magnitude larger than the CO (1→0) derived magnification of a spatially resolved Jansky Very Large Array (JVLA) map, using the same lens model. We estimate the quasar bolometric luminosity from a number of independent techniques and with our X-ray modelling find evidence that the AGN may be close to Compton thick, with an intrinsic bolometric luminosity of $\log_{10}(\langle L_{\rm bol,\,QSO}\rangle/{\rm L}_\odot) = 11.34 \pm 0.27$ dex. We make the first black hole mass estimate of IRAS F10214+4724 and find $\log_{10}(M_{\rm BH}/{\rm M}_\odot) = 8.36 \pm 0.56$ which suggests a low black hole accretion rate ($\lambda = \dot{M}/\dot{M}_{\rm Edd} \sim 3\pm^{7}_{2}$ per cent). We find evidence for an $M_{\rm BH}/M_{\rm spheroid}$ ratio that is one to two orders of magnitude larger than that of submillimetre galaxies (SMGs) at $z \sim 2$. At face value, this suggests that IRAS F10214+4724 has undergone a different evolutionary path compared to SMGs at the same epoch. A primary result of this work is the demonstration that emission regions of different sizes and positions can undergo significantly different magnification boosts (>1 dex) and therefore distort our view of high-redshift, gravitationally lensed galaxies.

Key words: gravitational lensing: strong – galaxies: active – galaxies: individual: IRAS F10214+4724.

1 INTRODUCTION

Two major empirical results in the last 15 years have greatly increased the need to characterize the black hole accretion history of the Universe, in particular in the redshift range $z \sim 2$–3 where the cosmic star formation and black hole accretion rate densities appear to peak (e.g. Dunlop & Peacock 1990; Madau et al. 1996). The first of these breakthroughs is the finding that supermassive black hole masses are strongly correlated with their host-galaxy spheroid luminosity and stellar velocity dispersion (Magorrian et al. 1998; Ferrarese & Merritt 2000; Gebhardt et al. 2000). The second is the realization that most ($\gtrsim$70 per cent) black hole accretion is obscured (e.g. Martínez-Sansigre et al. 2005; Gilli, Comastri & Hasinger 2007). Not only is the role of supermassive black holes more fundamental than previously thought, but our view of this fundamental process is largely hidden for the majority of active galaxies. This has driven a number of (necessarily multiwavelength) observation programmes to characterize this population of 'obscured' quasars, with a focus on the X-ray and mid-infrared (IR) windows (e.g. Polletta et al. 2006; Fiore et al. 2008). However, these regions of the electromagnetic spectrum have their challenges and contaminants,

⋆E-mail: roger.deane@astro.ox.ac.uk

© 2013 The Authors
Published by Oxford University Press on behalf of the Royal Astronomical Society

predominately due to Compton-thick column densities, the level of torus and/or host-galaxy obscuration and the unknown contribution of star formation to mid-IR dust heating. In this regard, high-resolution radio imaging provides a direct method of disentangling the AGN and star formation components through the measurement of brightness temperature and the radio spectral index.

This was demonstrated by Klöckner et al. (2009), who showed a sample of eleven $z \gtrsim 2$ obscured quasars to be radio intermediate-luminosity quasars ($L_{5\,\mathrm{GHz}} = 10^{23}-10^{24}$ W Hz^{-1} sr^{-1}), a challenging observation for very long baseline interferometry (VLBI) arrays. Until the previous decade, VLBI was an observational technique used almost exclusively to detect bright ($\gtrsim$10 mJy) radio sources which could be self-calibrated to improve the image quality and dynamic range. However, due to a confluence of factors – technical and scientific – VLBI has entered the sub-mJy domain.

In this work, we exploit the unique advantage of VLBI observations to isolate high brightness temperature emission at milliarcsecond scales and constrain the active core flux and position in a high-redshift, gravitationally lensed obscured quasar. While large-scale VLBI surveys will only be possible with the full Square Kilometre Array, current studies of individual systems (particularly lensed systems) provide a preview of the science that will be possible with a large sample size in a decade. In addition, a larger sample of unlensed systems from the *Herschel* ATLAS catalogue (Eales et al. 2010) have been observed with the European VLBI Network (EVN; Virdee et al., in preparation), a study that is important since it is free from any magnification bias and preferential magnification effects.

This paper is the third in a series on the gravitationally lensed, obscured quasar IRAS F10214+4724 (IRAS 10214 hereafter). IRAS 10214 is a well-studied galaxy that is often used as an archetype high-redshift ULIRG, largely because of its extensive multiwavelength coverage and its early discovery in 1991 (Rowan-Robinson et al. 1991). It radiates $\gtrsim$95 per cent of its bolometric luminosity in the IR, the intrinsic source of which is poorly constrained. IRAS 10214 is classified as a cusp-caustic lens that results in a large arc to the south of the lens galaxy and a small counter-image to the north of the lens (see Eisenhardt et al. 1996). In Deane et al. (2013, D13a hereafter), we derived a new lens model for IRAS 10214 based on a deep *Hubble Space Telescope* (*HST*) *F*814*W* map and introduced methods to investigate preferential magnification. In Deane et al. (2013b, D13b hereafter), we report a spatially resolved CO (1→0) Jansky Very Large Array (JVLA) observation that, by proxy, provides an estimate of the magnification of the star formation component in IRAS 10214.

In this work, we focus on the AGN properties of IRAS 10214. Previous observations have provided strong arguments that IRAS 10214 hosts an obscured quasar. The primary pieces of evidence supporting this are as follows.

(i) The observed optical continuum emission is highly polarized, implying that this is predominately scattered rest-frame ultraviolet (UV) light from a dust-embedded source (Lawrence et al. 1993).

(ii) Optical spectra show a wide range in ionization, supporting the view that the galaxy hosts an active nucleus (Elston et al. 1994; Soifer et al. 1995).

(iii) There are clear broad emission lines present in the polarized spectrum which are typical of quasars (Goodrich et al. 1996).

Despite these strong pieces of evidence, X-ray observations did not confirm the X-ray luminosity (L_{X}) expected in IRAS 10214, particularly when compared with the measured [O III]λ5007 luminosity which is correlated with L_{X} for type I AGN (Alexander et al. 2005; Iwasawa et al. 2009). These authors concluded that either the X-ray emission associated with IRAS 10214 was dominated by a dust-enshrouded starburst or the active nucleus was Compton thick ($\sigma_{\mathrm{T}} \gtrsim 10^{24}$ cm^{-2}).

The obscured nature of this quasar clearly makes it challenging to disentangle its emission from that of the host galaxy and reliably correct for extinction. In light of these challenges, we carried out VLBI observations which are unaffected by dust extinction and able to isolate high brightness temperature emission originating from an active radio core. Building on the previous multiwavelength work and incorporating the unique characteristics of VLBI observations, the aims of this paper are threefold.

(i) Detect the obscured active nucleus in a $z \sim 2$ radio-quiet quasar and hence estimate its contribution to the total radio flux.

(ii) Use the position to determine the AGN magnification. This is part of a wider case study of this high-redshift galaxy which also aims to quantify the scale of preferential lensing in this system, that is to say, the level of distortion in the spectral energy distribution (SED) that occurs due to different physical emission regions undergoing different magnification boosts. This is important in demonstrating the level of effective 'chromaticity' in strong gravitational lensing (due to the background source properties) which affects the physical interpretations of these systems.

(iii) VLBI imaging has the potential to solve a question that arose following the high-resolution *HST* imaging (Eisenhardt et al. 1996; Evans et al. 1999; Nguyen et al. 1999): is the UV/optical/near-infrared (NIR) arc in this system a single image or three images that are unresolved with the *HST* spatial resolution? The root cause of this debate stems from the two apparent peaks along the *HST F*814*W* and *HST F*437*M* arcs which could be an intrinsic source structure (i.e. clumpy UV emission as is typically observed in high-redshift galaxies) or multiple, partially resolved images.

This paper is structured as follows: in Sections 2 and 3 we describe the EVN observations and present the results. Section 4 reviews the UV polarization properties of IRAS 10214, while Section 5 investigates the source-plane position, magnification and multiwavelength context of the VLBI-detected source. In Sections 6 and 7 we estimate the quasar bolometric luminosity and black hole properties, and close with conclusions in Section 8. Throughout this paper, we assume a concordance cosmology of $\Omega_{\mathrm{M}} = 0.27$, $\Omega_{\Lambda} = 0.73$ and $H_0 = 71$ km s^{-1} Mpc $^{-1}$ (Spergel et al. 2007), which yields an angular size scale of 8.3 kpc arcsec^{-1} at the redshift of IRAS 10214 ($z = 2.2856$; Ao et al. 2008).

2 OBSERVATIONS

2.1 EVN 1.7 GHz

Observations of IRAS 10214 were made with the EVN at 1.66 GHz on 2010 November 2 and 3. Stations that were used in these observations included Jodrell Bank (76 m), Westerbork Radio Synthesis Array (phased array), Effelsberg, Onsala (26 m), Medicina, Torun, Cambridge, Knockin, as well as the three Russian outstations: Svetloe, Zelenchuk and Badary. This resulted in a baseline coverage of roughly 100–5000 km, corresponding to an angular scale range of 500–10 mas at an observing frequency of 1.66 GHz. It is for this reason that VLBI observations apply a brightness temperature filter which enables the unambiguous determination of the active core radio flux – one of the primary aims of this work. Observations were carried out with a 1024 Mbps recording rate in the standard continuum observing mode, employing eight 16 MHz subbands in each hand of polarization with two-bit sampling. The total

bandwidth of 128 MHz was centred on 1.658 99 GHz. Each sub-band was split into 32 channels of 500 kHz width. The integration period was set to 4 s. This results in a time- and bandwidth-smearing limited field of view of 0.24 and 0.34 arcmin^2, respectively. This is based on a metric that measures the angular displacement from the pointing centre at which a 10 per cent loss in the response to a point source is measured. These effective fields of view are larger than the optical/IR and molecular extent of IRAS 10214 by two orders of magnitude (D13b).

The total duration of the observations was 18 h, of which roughly 70 per cent was spent on the target. The observations were split into two 9 h runs that were performed on consecutive days. Given the IRAS 10214 1.7 GHz flux density of $S_{1.7} \sim 1$ mJy, as measured in D13a, the phase referencing technique was required. Through a separate EVN calibrator search we selected the $S_{1.7} \sim 70$ mJy source J1027+474 as the best possible phase calibrator for IRAS 10214 given its small angular separation of $\Delta\theta \sim 34$ arcmin. IRAS 10214 was observed for 8 min every 10 min, alternating with the phase calibrator. There was an additional cycle where the standard VLBA phase calibrator (J1027+4803) was observed for 4 min every hour. This was done to monitor the applied phase corrections and to check the resultant astrometric accuracy. 4C 39.25 was observed as a fringe finder. Since the observation was split into 2 × 9 h tracks, and the EVN has limited north–south coverage, the resulting beam pattern has a large ripple in the north–south direction (evident in Fig. 1).

Preliminary calibration of the *uv*-data set was carried out with the EVN automatic pipeline. This pipeline is written in ParselTongue (Kettenis et al. 2006), a high-level environment/interface for AIPS, and performs initial fringe fitting (calibration of delays, rates and phase), and phase and amplitude calibration. The latter are derived from system temperature measurements at individual stations. Following this preliminary calibration, a more detailed, manual calibration is performed in AIPS. This was performed in a cyclic process with detailed data editing, refined delay and rate calibration, as well as phase and amplitude self-calibration on the phase reference sources. Unfortunately, the majority of the observation on the second day was lost due to a combination of circumstances including strong winds, radio frequency interference, as well as the lack of several stations which did not take part (Effelsberg, Torun).

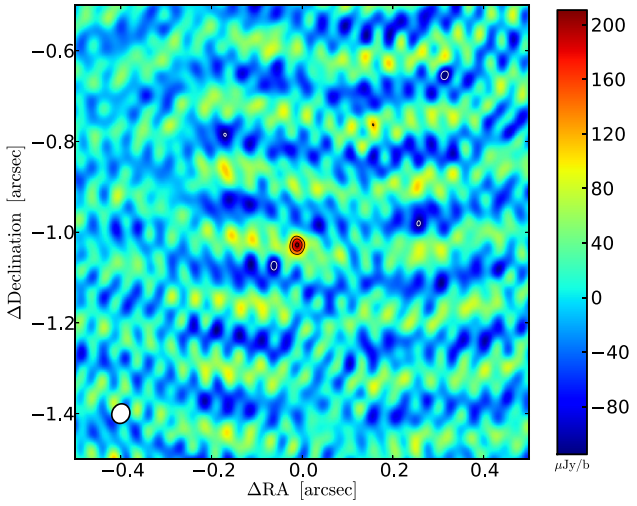

Figure 1. EVN 1.66 GHz continuum map of IRAS 10214. Overplotted are contours starting from -4σ, 4σ and increasing in steps of 2σ, where $\sigma = 23$ μJy per 44×39 mas^2 beam (white ellipse at bottom left, position angle $= -25.^\circ1$ east of north). The white contours indicate negative contours and the black contours indicate positive contours. The peak and integrated flux densities are $S_{\rm peak} = 209 \pm 23$ μJy and $S_{\rm int} = 220 \pm 37$ μJy. The *uv*-data are limited to a maximum of 5 $M\lambda$ based on the quality of the phase solutions derived from the phase calibrator. The observed noise structure results from the EVN synthesized beam. The map coordinates are centred on the lensing galaxy *HST F160W* centroid (RA $= 10^{\rm h}\,24^{\rm m}\,34.^{\rm s}5622$, Dec. $= 47^\circ\,09'\,10.''809$, see D13a).

All imaging was performed with the AIPS `imagr` task with a natural weighting scheme applied to the *uv*-data. Only after several rounds of the phase and delay calibration cycle (performed on the phase calibrator) did the noise level decrease to $\sigma \sim 23$ μJy beam^{-1} for an *uv*-range limited within 0–5 $M\lambda$. Including longer baselines (>5 $M\lambda$) improves the noise marginally (20 per cent); however, it results in large- and small-scale features that decrease the overall fidelity of the IRAS 10214 map. The reason for this decrease in image quality is due to the fact that the phase calibrator is spatially resolved on the longest baselines, leading to poor phase solutions. For this reason, we only consider baselines for which the phase calibrator is clearly unresolved (0–5 $M\lambda$).

The measured absolute position of the standard VLBA calibrator J1027+4803 is within $\Delta\theta < 0.80$ mas of its catalogued position. This was true for the preliminary pipeline calibration and for the manual delay and self-calibration performed in AIPS. The catalogued position uncertainties are ΔRA $= 0.28$ mas, ΔDec. $= 0.43$ mas, sourced from the International Celestial Reference Frame (ICRF-2). These two positions are consistent to within the submilliarcseond level, greatly exceeding the level of accuracy required in this work. The integrated flux density of J1027+4803 ($S_{\rm int} = 149 \pm 2$ mJy) is consistent with that derived by Helmboldt et al. (2007) with their VLBA 5 GHz observations ($S_{\rm int,\,5\,GHz} = 149.3 \pm 0.2$ mJy). VLBI resolution *L*-band observations of J1027+4803 have not been performed before prior to this work, so no direct flux density comparison is possible.

In addition, the radio coordinate reference frame must be directly compared to the optical reference frame. This has been performed by Lawrence et al. (1993), who compare the optical and radio positions of 20 compact radio sources in the region around IRAS 10214; however, they do not explicitly state the wavelength at which this comparison is done. They find no significant mean difference; however, they note that the error on the mean difference is 0.2 arcsec which we take as the systematic uncertainty in the radio–optical reference frame alignment. Greater detail is provided in Lawrence et al. (1993); however, since we use the same data, and our calibrators (as well as the 8 GHz centroids) are consistent, we assume that there is an equivalent astrometric matching between radio (1.7 and 8 GHz) and optical reference frames.

3 RESULTS FROM 1.7 GHZ VLBI MAP

In Fig. 1 we show the EVN 1.66 GHz CLEANed map with a 9σ detection. The peak flux density of the imaged data is $S_{\rm peak} = 209 \pm 23$ μJy. Fitting a Gaussian to the CLEANed map returns an integrated flux density of $S_{\rm int} = 220 \pm 37$ μJy, which suggests that the source is unresolved. The measured flux density and position of the detection were checked for a large number of subsets of the data, including splits in frequency, time and antenna selection. All these tests yield consistent positions and a flux density peak that ranges from $S_{\rm peak} \sim 190$ to 220 μJy. The positional uncertainty is $\sigma_\theta = 2.2$ mas, which is defined by $\sigma_\theta = 0.5\,{\rm FWHM}/({\rm S/N})$ (Condon 1997).

As shown in Fig. 2, the EVN detection does not appear exactly coincident with the *HST F814W* (rest-frame UV) peaks or

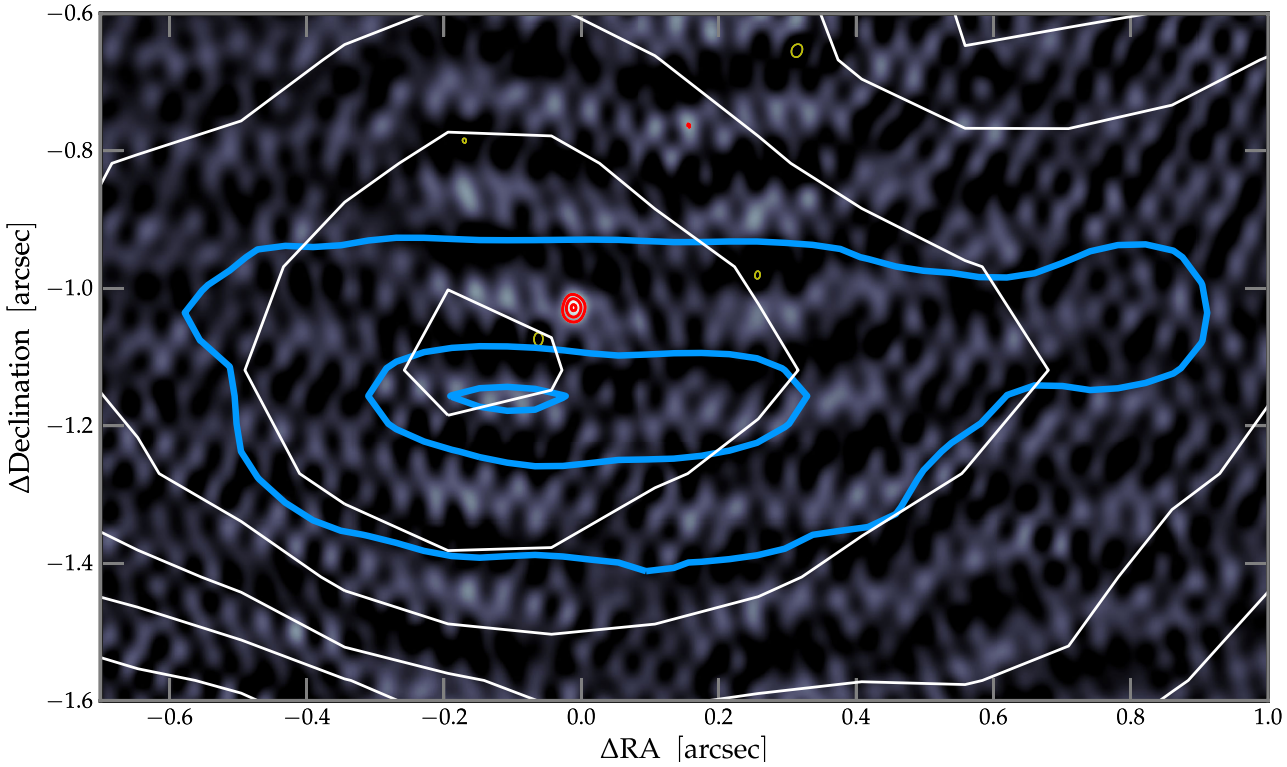

Figure 2. Zoomed-in view of the EVN 1.66 GHz continuum map from Fig. 1 with red *positive* contour levels at 4σ, 6σ, 8σ and yellow *negative* contours at -4σ. The CO (1→0) total intensity map is overplotted in white contours with 2σ intervals that start at -3σ, 3σ ($\sigma_{\rm CO} = 60$ μJy beam^{-1}). The blue contours show the *HST F*814*W* (rest-frame UV) arc at 2, 50, 95 per cent of the peak flux density. The CO (1→0) and *HST F*814*W* point spread functions are ∼0.7 and 0.1 arcsec, respectively. No additional EVN images appear to be present within the extent of the *HST F*814*W* arc.

the CO (1→0) total intensity map peak. First inspection shows that it lies roughly halfway along the main *HST F*814*W* arc (in RA) and >100 mas northwards of the centre of curvature. It is located ∼170 mas towards the north-west of the main (eastern) *HST F*814*W* peak. As discussed in D13a, the *HST* astrometry is in agreement with determinations from Nguyen et al. (1999), Eisenhardt et al. (1996), Evans et al. (1999) and Simpson et al. (in preparation) to within $\Delta\theta < 10$ mas.

3.1 Comparison with the *HST* image-plane configuration

The lensing configuration, detailed in D13a and briefly reviewed in Section 1, includes an arc at NIR wavelengths to the south of the lensing galaxy as well as a counter-image towards the north of the lens (see fig. 2, D13a). Our EVN observations here do not detect any emission in the region of the *HST F*814*W* and *HST F*160*W* counter-images. We place a weak, 5σ limit on the counter-image flux density of $S_{1.7,\rm min} \lesssim 100$ μJy since VLBI detections are generally only considered robust if greater than 5σ, due to poor *uv*-coverage.[1] We place the same detection limit for any potential emission that is co-located with the secondary CO (1→0)peak (labelled 'A' in D13b) and for the lensing galaxies identified in D13a (fig. 9). Note that these limits were obtained by shifting the phase centre to the *HST F*160*W* centroid in each case.

As stated in Section 1, one of the questions raised in the past is whether or not the *HST F*814*W* structure along the arc is intrinsic or whether there are multiple images that are convolved together by the *HST* point spread function (PSF). The *HST F*814*W* angular resolution was insufficient to unambiguously determine this; however, the higher angular resolution afforded by the EVN will determine if there is a radio core in the proximity of the *HST F*814*W* emission and more specifically if this radio core has multiple images within the *HST F*814*W* image-plane arc. These VLBI observations will therefore provide further constraints on the lens model, should a detectable radio core be present.

The relative magnification of these three split images would be defined by the cusp relation (e.g. Blandford et al. 1989; Keeton, Gaudi & Petters 2003), which states that the flux density of the two outer images should have a sum equal to the flux density of the central image. Therefore, if two outer images were present, they should *each* have a flux density of $S_{\rm outer} \sim 105$ μJy, equivalent to a 4.5σ detection in the EVN map. No evidence of additional images is present within the extent of the *HST* optical/NIR arc, as illustrated in Fig. 2 which shows the EVN map with overlaid *HST F*814*W* arc contours. The cusp relation does assume a smooth dark matter profile; however, a substructure does not appear to impact image magnification ratios substantially (e.g. McKean et al. 2007; More et al. 2009). Therefore, we assume that the EVN image plane is comprised of a main image (detected here at 9σ) and an undetected counter-image that is in the vicinity of the *HST*-detected counter-images.

4 UV POLARIZATION PROPERTIES

Polarization is a potential consistency check of a lens model, since theoretical arguments show that the polarization angle undergoes a negligible change in galaxy-scale lensing (i.e. in the weak field limit; Dyer & Shaver 1992). Since scattered light has a polarization angle

[1] Since our *uv*-coverage is comparatively good for a VLBI observation, 5σ is a relatively conservative upper limit.

Table 1. Flux-weighted mean polarization properties of IRAS 10214 from the literature.

Telescope	Bandpass (nm)	Polarization (per cent)	Position angle (°)	Reference
Keck	412–420	26.5 ± 1.7	69.9 ± 0.2	Goodrich et al. (1996)
Keck	750–800	15.9 ± 0.4	69.9 ± 0.2	Goodrich et al. (1996)
WHT	400–1000	16.4 ± 1.8	75 ± 3	Lawrence et al. (1993)
HST	*F*437*M*	28 ± 3	62 ± 2.7	Nguyen et al. (1999)

perpendicular to the vector between the source of the photons and the scattering clouds, we would therefore expect the vector between the AGN and scattering cloud(s) to have a position angle $\phi_{\rm pol} - 90^\circ$, where $\phi_{\rm pol}$ is the UV/optical polarization angle. In this section, we collate previous rest-frame UV polarimetry measurements and review the spatially resolved *HST* imaging polarimetry reported in Nguyen et al. (1999), before comparing the polarization with the derived source-plane properties of the EVN detection in Section 5.

A number of polarization observations have been performed towards IRAS 10214 (e.g. Lawrence et al. 1993; Goodrich et al. 1996; Nguyen et al. 1999), all of which report high polarization in the observed optical frame. A review of these results is summarized in Table 1 which shows that the shorter wavelengths have higher polarization percentages. From the three independent polarization angles listed in Table 1, we calculate the uncertainty-weighted mean polarization angle $\bar{\phi}_{\rm pol} = 68.9 \pm 1.3$ which we use in our analysis of the source plane in Section 5.

4.1 Polarization angle range

The polarization angle range reported in Nguyen et al. (1999) is $\Delta\theta_{\rm max} \sim 65^\circ$–$100^\circ = 35^\circ \pm 5^\circ$. A simplified argument is made in Nguyen et al. (1999) that assuming the source of the photons is a point source, and the diameter of the scattering region (D) is known, the projected distance between the scattering clouds and the photon source can be approximated by the formula $R \approx D\theta_{\rm max}$. They assumed magnifications of $\mu_{\rm UV} = 45$–250 to derive an intrinsic UV source diameter of $D = 40$–100 pc (presumably by dividing the apparent source solid angle by $\mu_{\rm UV}$). This results in an AGN projected distance estimate of $R = 160$–65 pc. These magnification estimates were based on the constrained range of arc to counter-image flux ratios (and magnification by proxy). Using the Markov Chain Monte Carlo derived (MCMC-derived) *HST F*814*W* source-plane diameter of $D = 2\,r_s = 720 \pm 180$ pc derived in D13a, section 4.1, we find a projected distance to the AGN of $R = 505 \pm 148$ pc. We note, however, that this is not a direct comparison since the $\Delta\theta_{\rm max}$ measurement is made in the *HST F*437*M* filter, while we have used the *HST F*814*W* radius. We argue that this is a reasonable approximation, since the arcs in both these filters have very similar lengths (∼0.7 arcsec) and unresolved widths. However, the *HST F*814*W* size is possibly an overestimate since the polarized emission is likely to be biased towards the brightest, and therefore more compact emission. Evidence for this claim can been seen in fig. 2 of Nguyen et al. (1999), which shows the extent of the polarized arc to be ∼0.55 arcsec long, after binning the 0.014 arcsec pixels into 0.042 × 0.14 arcsec bins. We also note that a more accurate distance may be achieved with a more complex *HST F*814*W* source model (rather than the circular Gaussian assumed in D13a, particularly given the fact that the arc is unresolved in the north–south direction).

The polarization angle range also provides another important piece of information. In principle, it enables a robust estimate of the ionization cone opening angle ($\phi_{\rm cone} = 0.5\,\Delta\theta_{\rm max} = 17.^\circ5 \pm 5^\circ$) assuming that the incident photons originate from a point source. The covering factor can therefore be calculated ${\rm CF} = 0.5\,\Delta\theta_{\rm max}/(\pi/2) = 0.195 \pm 0.028$ by spherical symmetry. We use this observational constraint in our bolometric luminosity estimates in Section 7.

5 SOURCE PLANE

We calculate the source-plane position of the EVN detection using the GLAMROC[2] software. We use Lens Model A, as defined in D13a. This assumes a singular isothermal ellipsoid potential for the main lens at $z = 0.893$ and a singular isothermal sphere potential for the secondary, line-of-sight galaxy at $z = 0.782$. IRAS 10214 is assumed to be a point source, which is consistent with the Gaussian fit presented in Section 3. The EVN source-plane coordinates are therefore the two remaining free parameters to solve for. We perform ray tracing of a point source from the source plane to the image plane, and minimize the predicted image-plane position with respect to the measured EVN position. The resultant magnification of the best-fitting point-source model is $\mu_{\rm EVN} = 68$. The magnification random error due to the ∼2 mas EVN positional uncertainty is of the order of 5 per cent (derived by adding a 2 mas dispersion to the trial model position prior to ray tracing), and therefore the systematic uncertainty of ∼40 per cent discussed in D13a (section 3.5) dominates the absolute magnification uncertainty. The EVN 1.7 GHz component magnification is therefore $\mu_{\rm EVN} = 68 \pm 3(\pm 27)$, where the systematic uncertainty is enclosed in parentheses. The EVN source-plane position is shown in Fig. 3.

Given the low probability that a small (<50 mas) source is located within <20 mas from the cusp of our lens model, we describe a number of consistency checks on the EVN source-plane position and its high magnification. First, the EVN source is northwards of the *HST* UV/optical arcs as stated in Section 3 and does not split into three images (at 4.5σ significance, see Section 3); therefore, it is most likely to the south of (or on) the cusp of the caustic. Secondly, the EVN detection is positioned roughly along the vector that extends from the centre of the lens and bisects the angle subtended by the rest-frame UV/optical arcs. This implies that the source-plane position must be very close (< few milliarcseconds) to the cusp of the caustic, since this is a region with large tangential deflection angles. The EVN point source is therefore essentially 'wedged' between the inner caustic and the *HST* UV/optical arc, which will always result in high magnifications regardless of changes in the macroscopic lens model. In Fig. 4, we plot the predicted total magnification as a function of intrinsic source radius, assuming the source is centered on the EVN source plane position.

[2] Gravitational Lens Adaptive Mesh Raytracing of Catastrophes, see http://kipac.stanford.edu/collab/research/lensing/glamroc

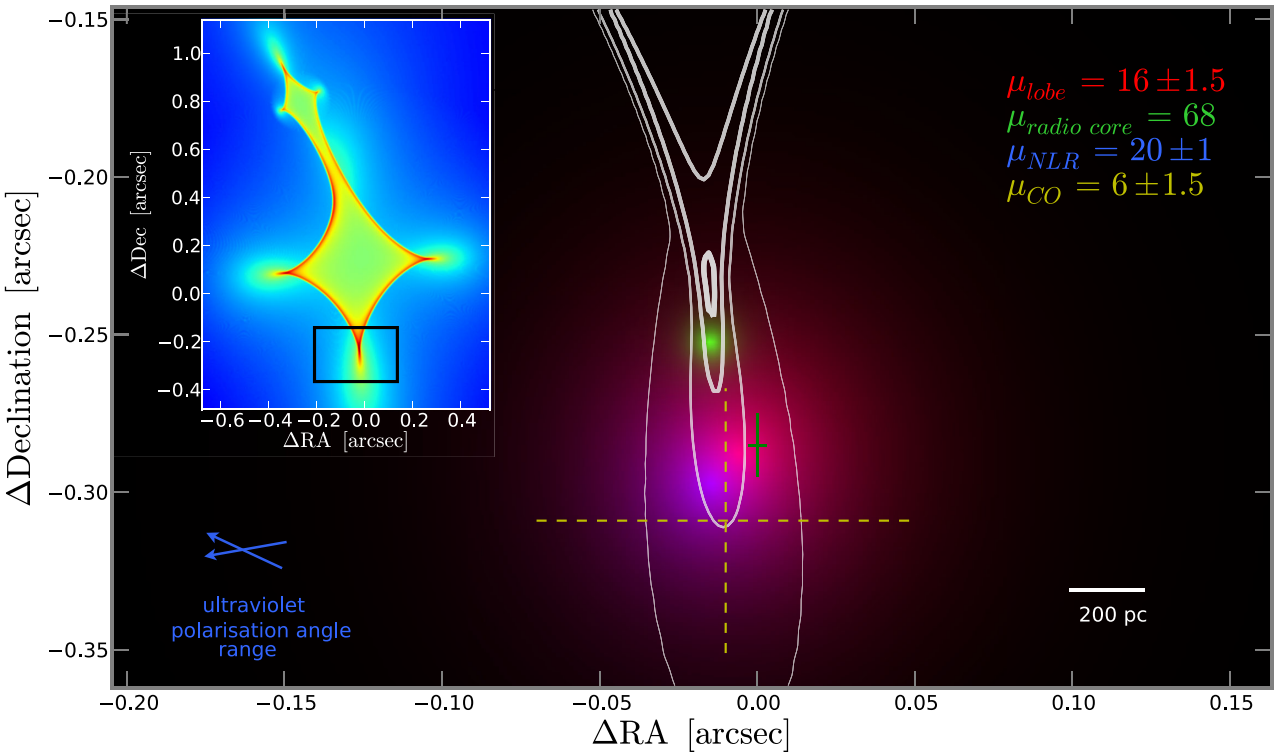

Figure 3. Source-plane reconstruction of IRAS 10214 showing the radio core (green, EVN 1.7 GHz), scattered quasar light (blue, *HST F*814*W*) and radio lobe (red, MERLIN 1.7 GHz). The yellow dashed cross shows the CO (1→0) total intensity map source-plane centroid and its uncertainty [the extent of the source-plane CO (1→0) component is beyond this entire frame]. The green cross indicates the 8 GHz map source-plane centroid and its uncertainty. The white contours represent lines of equal magnification extending from the caustic at levels μ = 10, 20, 50, 100. The blue arrows (bottom left) depict the range of UV polarization angles along the *HST F*437*M* arc. The inset shows the full lens caustic with colour scale representing magnification and the black rectangle showing the borders of the enlarged region.

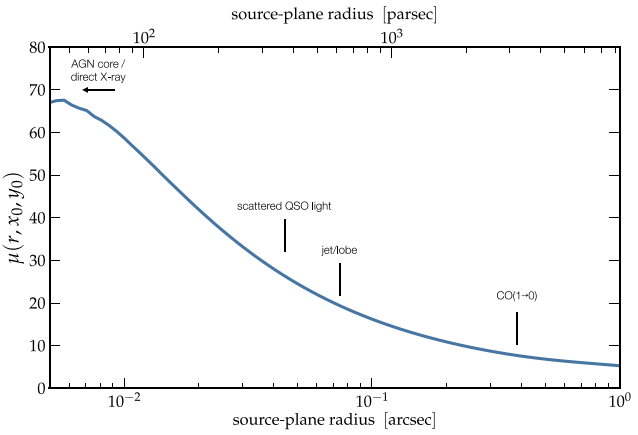

Figure 4. Total magnification as a function of the source-plane scale radius, assuming the EVN source-plane centroid. The annotations serve as a rough guide of the physical sizes. The centroids of the listed components are not the same as the EVN component and therefore the resultant magnifications are marginally different. The point-source magnification at the best-fitting EVN position is $\mu_{\rm EVN} = 68$.

Assuming that the EVN point source is the obscured active nucleus, its source-plane position is consistent with a number of multiwavelength observations outlined below.

(i) Simpson et al. (in preparation) present two narrow-band maps centred on the redshifted C IV and [O III] lines, which are typical broad-line region (BLR)and narrow-line region (NLR) emission lines, respectively. They determine the centres of curvature of both and find that the C IV arc is roughly 50±20 mas northwards of the [O III] centre of curvature for the highest S/N bins. At face value, this implies that the BLR (or scattered BLR light) is northwards of the NLR, which in our D13a model is one sided. This is consistent with resolved NLR imaging performed in the local Universe (Liu & Pooley 1991; Simpson et al. 1997) and implies that the active nucleus is northwards of the NLR and *HST F*814*W* centres of curvature. The relative configuration of the emission associated with the BLR and NLR is therefore consistent with the source-plane EVN position, if it traces an obscured active nucleus.

(ii) Comparison of the source-plane UV and radio core positions shows that the median UV polarization angle ($\langle\phi_{\rm pol}\rangle = 82.^{\circ}5 \pm 5^{\circ}$, with a range ∼65°–100°) is roughly perpendicular to the vector connecting the EVN radio core and *HST F*814*W* source-plane centroids ($\phi_{\rm core,\,uv} \sim 0^{\circ}$). This supports the view that the EVN detection is the dust-embedded source that emits the scattered, and therefore polarized, UV/optical radiation.

(iii) The lensing inversion predicts that the EVN and *HST F*814*W* source-plane centroids are separated by a distance $R = 370 \pm 148$ pc, where the uncertainty is dominated by the absolute magnification uncertainty. As calculated in Section 4, the projected distance between the AGN and the scattered UV light is $R = 505 \pm 145$ pc, which is based on the UV polarization angle range ($\Delta\theta_{\rm max} = 35^{\circ} \pm 5^{\circ}$) and the predicted *HST F*814*W* source-plane radius ($r_{\rm s} = 360 \pm 90$ pc). The two independently calculated projected distances between EVN and *HST F*814*W*

source-plane centroids are therefore consistent with one another.

The lensing inversion places the EVN-detected radio core at a position qualitatively consistent with the Nguyen et al. (1999) prediction of the AGN position. This is a promising example of the potential held by high-sensitivity, high-resolution spectropolarimetry with next-generation 30–40 m optical/IR telescopes in accurately locating the obscured active nuclei in high-redshift galaxies.

6 DISCUSSION

6.1 AGN core or highly magnified star formation clump?

At first glance, the EVN detection is likely to be the AGN radio core; however, careful consideration is required given the close proximity of the cusp of the caustic. IRAS 10214 was discovered at $\lambda_{\rm obs} = 100\,\mu$m, a wavelength biased towards warm, partially AGN-heated ($T \sim 100$ K) dust. This is consistent with its AGN features across the spectrum and so the close proximity of an AGN core to the cusp would be expected. However, the probability that such a compact point source is within a few milliarcseconds of the cusp is low. We must consider an alternative scenario where the EVN detection is co-spatial with a star-forming complex with an exceptionally large magnification ($\mu > 100$). This potentially has a higher probability, given the supernova rate we expect from the large star formation rate (SFR) in IRAS 10214 (SFR $> 100\,{\rm M}_\odot\,{\rm yr}^{-1}$) and therefore the number of star formation clumps.

We calculate the brightness temperature of the EVN-detected emission using equation 6 of D13a. We assume a solid angle equal to the area of the beam effective radius [i.e. $\Omega_{\rm beam} = \pi\ \frac{1}{2}\theta_{\rm maj}\ \frac{1}{2}\theta_{\rm min}$, where $\theta_{\rm maj,\,min}$ are the full width at half-maximum (FWHM) values of the beam]. The peak flux density is $S(\nu_{\rm o}) = S_{\rm peak} = 209\,\mu$Jy, which results in a rest-frame 5.45 GHz brightness temperature lower limit of $T_{\rm B} > 5 \times 10^5$ K, since the source is unresolved. This lower limit seems to rule out a significant contribution from star formation, which appears to saturate at $T_{\rm SF}^{\rm max} \sim 10^5$ K (Muxlow et al. 1994). Note that these calculations do not depend on the magnification as the surface brightness, and hence the brightness temperature, is not affected by gravitational lensing.

More distinguishing is the implied SFR density ($\Sigma_{\rm SFR}$) if we assume that the EVN-detected flux density is associated with star formation. Using equation 7 of D13a, we calculate the implied SFR assuming that all the emission is due to star formation. We assume a 1.7 GHz flux density $S_{\rm peak} = 209\,\mu$Jy, a spectral index $\alpha = 0.8$ and set the intrinsic source size equal to the EVN 1.7 GHz beam. This results in a lower limit of $\Sigma_{\rm SFR} > 8.4 \times 10^4\,{\rm M}_\odot\,{\rm yr}^{-1}\,{\rm kpc}^{-2}$. This is significantly larger than the theoretically motivated and observationally supported value of $\Sigma_{\rm SFR}^{\rm max} \sim 1000\,{\rm M}_\odot\,{\rm yr}^{-1}\,{\rm kpc}^{-2}$ (see Scoville, Yun & Bryant 1997; Downes & Solomon 1998; Elmegreen 1999; Thompson, Quataert & Murray 2005). These arguments, in addition to those presented in Section 5, appear to support that this is an AGN core, which is what we assume for the remainder of the paper. As argued in Section 5, this is consistent with a number of multiwavelength and rest-frame UV polarization properties.

6.2 Nature of VLA 8 GHz map peak

In D13a, we suggested that the VLA 8 GHz map could potentially be dominated by a radio core, based on the radio spectral index behaviour from 330 MHz through 16 GHz. However, the 8 GHz centroid is significantly offset from the EVN detection presented here (see Fig. 5), with a separation of $\Delta\theta \sim 300 \pm 20(\pm 200)$ mas,

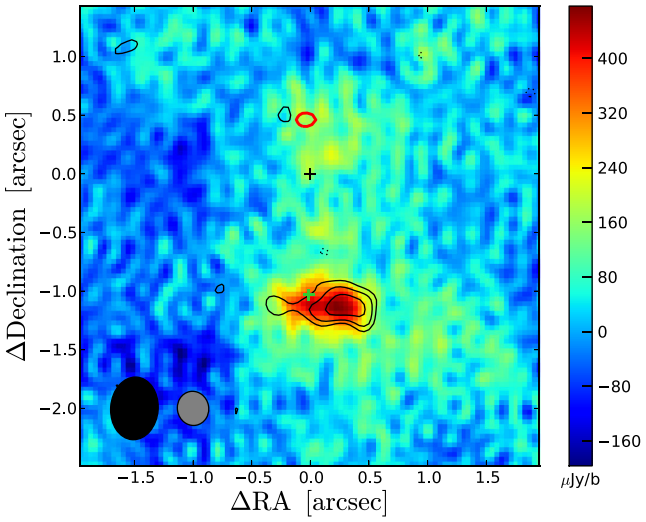

Figure 5. MERLIN 1.7 GHz map shown in colour scale with $\sigma \sim 46\,\mu$Jy per 405×349 mas^2 beam (position angle $= -4\overset{\circ}{.}35$). Overplotted in black contours is the 8 GHz VLA map with $\sigma \sim 11\,\mu$Jy per 292×267 mas^2 beam (position angle $= -79\overset{\circ}{.}64$). Contours are at $\pm 3\sigma$ and increase by a factor of $\sqrt{2}$. The dashed lines represent the negative contours. The MERLIN and VLA beams are illustrated in the bottom-left corner as black and grey ellipses, respectively. The green cross indicates the location of the EVN-detected radio core, where the cross length is a factor of $\gtrsim$10 larger than the EVN positional uncertainty. The red ellipse towards the north shows the *HST F814W* counter-image contour. The black cross indicates the Sérsic-fitted centroid of the lensing galaxy as measured from the *HST F160W* map.

where the first uncertainty is the quadrature sum of the two random position uncertainties (8 GHz discussed in D13a) and the second uncertainty in parentheses is the systematic uncertainty based on the radio–optical reference frame alignment. The nature of the 8 GHz emission is puzzling, since we expect it to be co-located with the EVN detection, especially since their flux densities are very similar ($S_{8\,\rm GHz} = 280\,\mu$Jy), assuming a flat radio spectrum. It does not seem that this discrepancy can be discarded on the basis of insufficient astrometric accuracy. This is because the 8 GHz centroid was measured for two independent observations performed in 1991 and 1995, both with the VLA in A-configuration and hence a resolution of $\theta_{\rm syn} \sim 0.23$ arcsec. As discussed in Section 2.1, the astrometry of the EVN map appears secure to within $\lesssim$2 mas. The true nature and extent of the 8 GHz emission will be further probed by a *C*-band JVLA polarization observation of IRAS 10214 in A-configuration ($\sim$30 mas angular resolution) with 2 GHz bandwidth. With the EVN map, we can estimate a 5σ limit on the spectral index of the 8 GHz peak of $\alpha < -0.54$, assuming that it is a point source and defining $\alpha \equiv -\log(S_1/S_2)/\log(\nu_1/\nu_2)$.

6.3 Resolved-out radio emission

The radio core flux is $\sim$20 per cent of the total flux in the 1.7 GHz MERLIN map presented in D13a. If we assume that the remaining flux is associated with star formation and a spectral index $\alpha = 0.8$, the implied star formation rate is SFR $\sim 3.2 \times 10^4\,\mu^{-1}\,{\rm M}_\odot\,{\rm yr}^{-1}$ following equation 7 of D13a. If the MERLIN 1.7 GHz magnification ($\mu_{1.7} = 16 \pm 1.5$) derived in D13a is assumed to be equivalent to the star formation magnification, then this results in an intrinsic star formation rate of SFR $\sim 2 \times 10^3\,{\rm M}_\odot\,{\rm yr}^{-1}$. This is an exceptional SFR, which suggests that there may be significant flux in the radio

jet/lobe components that are resolved out by the EVN observations. It is unlikely that the total magnification boost of the star formation emission region is higher, since any disc with a reasonable star formation size ($\gtrsim$1 kpc) undergoes a magnification boost of $\mu \lesssim 10$.

7 QUASAR BOLOMETRIC LUMINOSITY

Having detected the radio core and made an estimate of its magnification, we now wish to use these results to estimate the quasar bolometric luminosity in IRAS 10214 using five methods in the X-ray, UV and mid-IR

7.1 [O III] equivalent width $L_{\rm bol}$ estimate

The first method uses the equivalent width (EW) of the forbidden [O III] λ5007 line to measure the 'missing' optical continuum flux as a result of the obscuring geometry (Miller et al. 1992). Their method measures the average [O III] EW of 76 type I quasars from the Bright Quasar Survey (BQS), which provides a way to estimate the obscured AGN continuum flux, and hence the extinction. The idea is that the NLR flux will be largely unaffected by the orientation of the quasar since it is above and beyond the putative torus, whereas the central AGN continuum would be obscured in the unified quasar model (Antonucci 1993). Since the EW measures the fraction of energy of a spectral line relative to the underlying continuum, the greater the central AGN obscuration, the more exaggerated the EW of a narrow line like [O III] will be from its intrinsic value.

Miller et al. (1992) measure an average rest-frame [O III] equivalent width $\langle {\rm EW} \rangle_{\rm O\,III} = 24 \pm^{25}_{12}$ Å for their BQS sample. Serjeant et al. (1998) measure the [O III] rest-frame EW of IRAS 10214 to be ${\rm EW}_{\rm O\,III} = 580\,(1+z)^{-1} = 176$ Å. Two approaches can now be followed to estimate the bolometric luminosity. The first simply assumes that given a measurement of the [O III] line flux density, one can estimate the bolometric luminosity with the relation

$$L_{\rm bol,O\,III^1} \;=\; L_{\rm O\,III}\,\mu^{-1}_{\rm NLR}\,{\rm BC}, \qquad (1)$$

where $L_{\rm O\,III} = 2.05 \times 10^{37}$ W (Lacy, Rawlings & Serjeant 1998; Serjeant et al. 1998), $\mu_{\rm NLR} = 20 \pm 1$ is the NLR magnification derived in D13a from the *HST F*814*W* map, and BC = 89.9 is a bolometric correction factor calculated from the average quasar [O III] EW (Miller et al. 1992) and a correction factor to convert the specific luminosity at 5100 Å to a bolometric luminosity (Elvis et al. 1994). This results in a bolometric luminosity estimate of $L_{\rm bol,O\,III^1} = 2.4 \pm 0.6 \times 10^{11}\,{\rm L}_\odot$.

The second estimate, $L_{\rm bol,O\,III^2}$, is less direct. It extrapolates an optical continuum flux based on a dust-reddened quasar SED fit to the UV flux data points. Scattered QSO light is presumed to dominate the latter. By comparison of the observed IRAS 10214 and average quasar [O III] EW, the argument can be made that only $13.6 \pm^{14}_{6.8}$ per cent of the AGN core continuum emission is observed at 5100 Å. This is calculated by taking the ratio ${\rm EW}'_{\rm O\,III}/\langle {\rm EW} \rangle_{\rm O\,III}$, where ${\rm EW}'_{\rm O\,III}$ is the measured [O III] equivalent width and $\langle {\rm EW} \rangle_{\rm O\,III}$ is the average [O III] equivalent width (Miller et al. 1992). Therefore, we can estimate the true specific luminosity at 5100 Å] as follows:

$$L_{5100,\rm true} = L'_{5100,\rm obs}\,\frac{{\rm EW}'_{\rm O\,III}}{\langle {\rm EW} \rangle_{\rm O\,III}}$$

$$= L_{5100,\rm obs}\,\mu^{-1}_{5100}\,\frac{{\rm EW}_{\rm O\,III}}{\langle {\rm EW} \rangle_{\rm O\,III}}\,\frac{\mu_{5100}}{\mu_{\rm NLR}}, \qquad (2)$$

where $L'_{5100,\rm obs}$ is inferred from the lensed, host-galaxy-reddened *quasar* flux density at 5100 Å, $L'_{5100,\rm obs} = 1.9 \times 10^{23}$ W Hz^{-1}, $\mu_{5100}/\mu_{\rm NLR}$ accounts for the difference in magnification between the NLR and the AGN nucleus, and ${\rm EW}_{\rm O\,III}$ is the equivalent width in the absence of differential lensing effects. Note that $\mu_{5100} = \mu_{\rm AGN}$ since we are interested in the specific luminosity of the quasar at 5100 Å.

To calculate $L'_{5100,\rm obs}$, we fit the average quasar spectrum (Elvis et al. 1994) to the 11 UV photometric points within rest-frame 1000–2750 Å and extrapolate to 5100 Å since this wavelength is dominated by stellar emission as discussed in D13a and Section 8.2. This includes the *HST F*814*W* photometric point and is therefore assumed to be scattered quasar emission given the high degree of polarization. The UV photometric points are reddened by a range of dust models from Pei (1992) to account for *host-galaxy* extinction, since this is scattered QSO light. The fit results in a best-fitting visual extinction $A_V = 0.18$ with a Small Magellanic Cloud dust grain model, with a $\chi^2_\nu = 1.3$. The extinction is comparable to the $A_V \sim 0.3$ from Lacy et al. (1998) towards the NLR based on the He II 468.6/164.0 ratio of 4.3). The best-fitting extinction, bolometric luminosity and χ^2_ν have very little variance with subsets of the UV photometric points (from 4 to 11); however, the goodness of fit begins to decrease substantially once the optical photometry is included, as one would expect with a significant stellar component. The full resolution UV spectrum from which these photometry points originate has a continuum baseline that Rowan-Robinson et al. (1993) fit with two linear models which meet at $\lambda_{\rm rest} \sim 2600$ Å. This supports our selection of fitting boundaries, as well as the goodness of fit behaviour as this boundary is extended into optical wavelengths. The reddened quasar fit to the observed UV spectrum is plotted in Fig. 6.

This implies a bolometric luminosity $L_{\rm bol,O\,III^2} = 1.9 \pm^{2.0}_{1.0} \times 10^{39}\,\mu^{-1}_{5100}\,\mu_{5100}/\mu_{\rm NLR}$ W, since $L_{5100,\rm true} = L_{\rm O\,III}/(24 \pm^{25}_{12})$ as determined for unobscured quasars in Miller et al. (1992). Assuming our previously derived magnification factors, this leads to $L_{\rm bol,O\,III^2} = 2.8 \pm^{2.8}_{1.4} \times 10^{11}\,{\rm L}_\odot$, which is 16 per cent greater than the first $L_{\rm bol,O\,III^1}$ method. We adopt the average of the

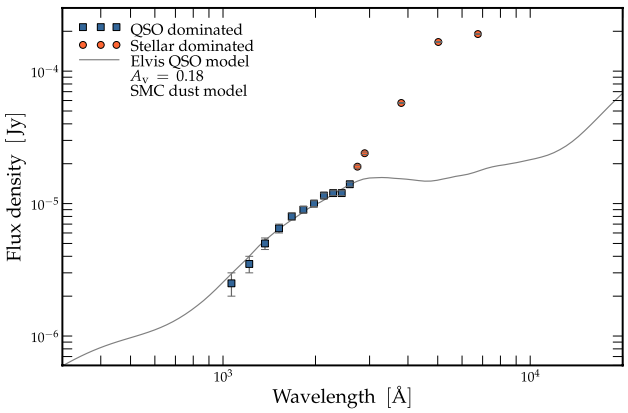

Figure 6. UV fit to a reddened quasar model. The dust extinction model is from Pei (1992) and the intrinsic quasar model is an average from the sample of Elvis et al. (1994). Only the blue squares are included in the fit as these are presumed to be dominated by scattered quasar light, as suggested by the high degree of polarization. We argue that the orange circles are dominated by the host-galaxy's stellar component which is supported by the lower magnification seen at rest-frame optical/NIR wavelengths (as surmised from lower arc to counter-image flux ratios).

two and note that the uncertainty is dominated by the $\langle \mathrm{EW} \rangle_{\mathrm{O\,III}}$ scatter. The result is $L_{\mathrm{bol,O\,III}} = 2.6 \pm^{2.6}_{1.3} \times 10^{11}\,\mathrm{L}_{\odot}$.

7.2 UV L_{bol} estimate

The scattered quasar light we observe is of course a fraction of the total quasar light. If we can determine the covering factor and appropriate magnification, then we can determine the intrinsic quasar bolometric luminosity. The magnification is reasonably assumed to be $\mu_{\mathrm{NLR}} = 20 \pm 1$ since the *HST F*814*W* observation directly probes the emission assumed to be dominated by the scattered quasar light. The covering factor ($\mathrm{CF} = 0.195 \pm 0.028$) is approximated by the maximum change in the polarization angle ($\Delta\theta_{\mathrm{max}}$) of the scattered UV light as discussed in Section 4. The luminosity at 2400 Å (rest-frame *HST F*814*W*) is $\nu L_{2400} = 5 \pm 2 \times 10^{11}\,\mathrm{L}_{\odot}$. We also account for host-galaxy extinction ($A_V = 0.18$) based on the modelling described in Section 7.1. This leads to a UV bolometric luminosity estimate of $L_{\mathrm{bol,UV}} = L_{2400}\,\mathrm{BC}_{2400\,\text{Å}}\,10^{A_V/2.5}/\mu_{\mathrm{NLR}} = 2.7 \pm 1.1 \times 10^{11}\,f^{-1}_{\mathrm{scatt}}\,\mathrm{L}_{\odot}$. The scattering fraction f_{scatt}, which is poorly constrained, will increase the derived value if much smaller than unity. We are fairly ignorant of the true f_{scatt} value, and plot the $L_{\mathrm{bol,\,UV}}$ estimate in Fig. 8 (green line) assuming $f_{\mathrm{scatt}} = 100$ per cent.

7.3 Mid-IR L_{bol} estimates

Spitzer mid-IR spectroscopy has proved a powerful technique to probe the heart of quasar host galaxies through dust heating and spectral features. In the case of IRAS 10214, the mid-IR spectrum is best fitted with three components: (1) a typical star-forming dust temperature of 50 K, (2) a warm 210 K component and (3) a hot 600 K component (see Efstathiou 2006; Teplitz et al. 2006). We motivate appropriate covering factors and magnifications for the latter two components which we expect are predominately heated by the central AGN. This will allow additional estimates of the intrinsic bolometric luminosity.

7.3.1 600 K dust

Efstathiou (2006) fit a 600 K component to the mid-IR spectrum that has an apparent bolometric luminosity $L_{\mathrm{bol,600\,K}} = 7.4 \times 10^{11}\,\mathrm{L}_{\odot}\,\mathrm{CF}^{-1}_{600\,\mathrm{K}}\,\mu^{-1}_{600\,\mathrm{K}}$. The covering factor ($\mathrm{CF}_{600\,\mathrm{K}}$) and magnification ($\mu^{-1}_{600\,\mathrm{K}}$) at this temperature do not represent that of a distinct physical component, but rather a representative average of the hot dust component. We contend that this 'component' is located within ∼50 pc of the radio core and therefore has a mean magnification of $\mu_{600\,\mathrm{K}} \sim 68$, as inferred from Fig. 4. The distance limit is based on mid-IR interferometric (using VLTI) size limits from nearby Seyfert galaxies (Tristram et al. 2009; Tristram & Schartmann 2011). These authors find a size–luminosity relation $s = p\,L^{0.5}$, where $p = 1.8 \pm 0.3 \times 10^{-18}$ [pc $\mathrm{W}^{-0.5}$]. This implies a torus size of the order of $s = 30{-}55$ pc for IRAS 10214 for range of quasar bolometric luminosities determined for $L_{\mathrm{bol,\,UV}}$ and $L_{\mathrm{bol,O\,III}}$. The covering factor for this component is set to the value derived in Mor, Netzer & Elitzur (2009), who model the mid-IR spectra of 26 luminous QSOs with three dust components: (1) a clumpy torus, (2) a dusty NLR and (3) a hot blackbody representing the hottest dust around the nucleus. A 600 K dust component would clearly be associated with the last of these three components, for which the authors find a mean covering factor $\langle \mathrm{CF} \rangle = 0.23 \pm 0.1$. This covering factor compares well with our adopted value $\mathrm{CF} = 0.195 \pm 0.028$ which is based on the maximum change in the polarization angle. Based on the polarization-determined covering factor and magnification, we estimate a bolometric luminosity $L_{\mathrm{bol,600\,K}} = 4.8 \pm^{5}_{2.2} \times 10^{10}\,\mathrm{L}_{\odot}$.

7.3.2 210 K dust

This bolometric luminosity estimate follows the same reasoning as the 600 K component; however, the average distance of clouds contributing to this temperature is greater than that of the hotter, 600 K dust and therefore likely to undergo a different amplification boost. The peak rest wavelength of this component is 14 μm, just longwards of the 10 μm silicate feature. Based on evidence from silicate *emission* in type 2 Seyferts (e.g. Shi et al. 2006; Sturm et al. 2006), as well as resolved silicate imaging on ∼100 pc scales (Schweitzer et al. 2007), it appears that the ∼10 μm emission may be dominated by a combination of outer torus and NLR dust cloud emission. Following the multicomponent mid-IR modelling of Mor et al. (2009), who find a correlation between the NLR cloud distance and bolometric luminosity, we estimate an NLR distance of $r_{\mathrm{NLR}} = 125 \pm^{35}_{25}$ pc based on the range of values derived for $L_{\mathrm{bol,\,UV}}$ and $L_{\mathrm{bol,O\,III}}$.

We make the simplified argument that the 210 K component has a 125 pc radius, the same covering factor as derived before ($\mathrm{CF} = 0.195 \pm 0.028$), and is centred on the EVN point source which results in a magnification $\mu_{210\,\mathrm{K}} \sim 50$ (from Fig. 4). Efstathiou (2006) and Teplitz et al. (2006) find a 210 K component bolometric luminosity of roughly $L_{\mathrm{bol,210\,K}} = 5.5 \times 10^{12}\,\mathrm{L}_{\odot}\,\mathrm{CF}^{-1}_{210\,\mathrm{K}}\,\mu^{-1}_{210\,\mathrm{K}}$. We therefore find $L_{\mathrm{bol,\,210\,K}} = 5.6 \pm 3 \times 10^{11}\,\mathrm{L}_{\odot}$ from the assumptions above. This is higher than the other bolometric estimates, especially that based on the 600 K dust. This could be expected since some, potentially large, fraction of the 210 K dust heating will arise from the prodigious star formation in IRAS 10214. An estimate of this contribution is the fraction of luminosity an 80 K greybody (i.e. dust primarily heated by star formation, and roughly where the IRAS 10214 mid-IR spectrum peaks) contributes at $\lambda = 14$ μm, the wavelength that corresponds to the peak of a 210 K greybody. The 80 K component contributes 1.5 per cent assuming equal peak luminosities for the two temperature components. Previous work has shown that the star formation dominates the bolometric luminosity of IRAS 10214 at the >90 per cent level (e.g. Rowan-Robinson et al. 1991; Efstathiou 2006; Teplitz et al. 2006). If we assume a star formation to quasar L_{bol} ratio in the 90–95 per cent range, then an 80 K greybody contributes ∼15–30 per cent to the flux at 14 μm (210 K peak wavelength). This suggests that the $L_{\mathrm{bol,\,210\,K}}$ estimate is significantly contaminated by star formation.

7.4 X-ray L_{bol} estimate

This method uses an X-ray spectrum fit employing the models of Wilman & Fabian (1999) to find the best-fitting column density of intervening hydrogen (N_{H}). The X-ray models are Monte Carlo derived and assume an intrinsic unobscured type I quasar X-ray spectrum of the form $L_{\nu} \propto \nu^{-0.9}\,\mathrm{e}^{-\nu/\nu_{\mathrm{c}}}$ (where $h\nu_{\mathrm{c}} = 360$ keV), as described in Madau, Ghisellini & Fabian (1994). Wilman & Fabian (1999) generated a library of models with a range of hydrogen column densities (N_{H}), assuming five times solar metallicity as they find that this provides a superior fit to the hard X-ray background which peaks at ∼30 keV. The models further assume a 2 per cent flux component that is scattered off the central ionized medium. For simplicity, we do not consider models that include a reflection component off an accretion disc. In our MCMC routine, we include a dispersion on the scattered percentage with FWHM = 10 per cent

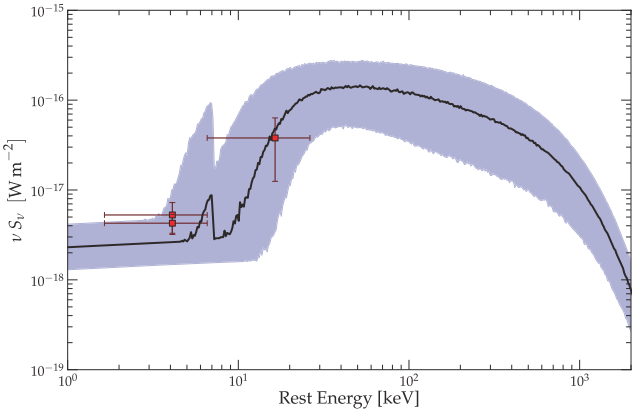

Figure 7. Best-fitting X-ray model spectrum to the *Chandra* and *XMM–Newton* space telescopes. The shaded region corresponds to the 68 per cent confidence levels of the hydrogen column density ($N_{\rm H}$) and quasar bolometric luminosity ($L_{\rm bol}$). The bands correspond to 0.5–2 and 2–8 keV.

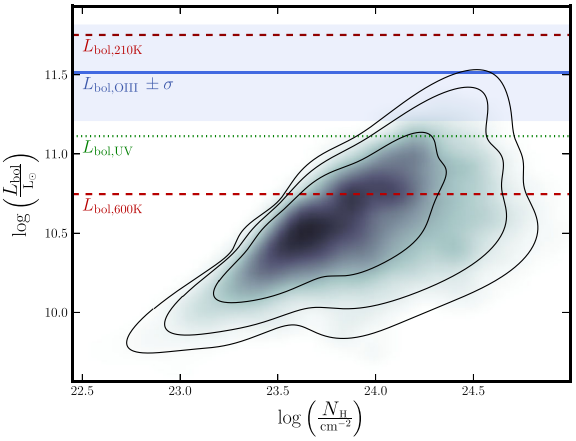

Figure 8. Two-dimensional posterior PDF assuming the Wilman & Fabian (1999) X-ray model spectra. The contours correspond to 68, 95 and 99 per cent confidence levels. The blue line indicates the bolometric luminosity as derived from the [O III] EW and the blue shaded horizontal band corresponds to the associated 1σ uncertainty. The two dashed red lines indicate the two dust bolometric luminosity estimates, while the green dotted line shows the UV $L_{\rm bol}$ estimate. Note that the Compton limit is $\sim 10^{24}$ cm^{-2}. For clarity, we have not included the $L_{\rm bol,\,UV}$, $L_{\rm bol,\,210\,K}$ and $L_{\rm bol,\,600\,K}$ uncertainties. They are dominated by the quadrature sum of the covering factor and magnification uncertainties and are of the order of 0.3–0.5 dex.

(in the range 0–100 per cent). Although Wilman & Fabian (1999) assume a fixed scattering fraction, we wish to decrease the sensitivity to this assumption, particularly as they note that there is likely some dispersion in this quantity, as suggested by high IR luminosity ($L \gtrsim 10^{13}$ L$_\odot$) *IRAS* galaxies observed with the *ROSAT* high-resolution imager, that place upper limits on the 0.1 ± 2.4 keV fluxes and imply scattering fractions below ∼0.5 per cent (Fabian et al. 1996; Wilman et al. 1998). While the selection of a 10 per cent dispersion FWHM for our MCMC chains is relatively arbitrary, it gives practically the same probability to the lower values for luminous IR galaxies reported above, whilst also opening up the parameter space to incorporate the effect of higher values.

The resulting models are compared to the X-ray observations of IRAS 10214 with both *Chandra* and *XMM–Newton* space telescopes (which have consistent, albeit low-S/N, results). Samples of the posterior Probability Distribution Function (PDF) of the hydrogen column density $N_{\rm H}$ and bolometric luminosity $L_{\rm bol}$ are drawn in an MCMC algorithm similar to that described in D13a. Fitting a library of X-ray models to the three X-ray data points is a weakly constrained problem, and so an important caveat to these results is that we assume a hydrogen column density prior $N_{\rm H}$ with a mean of 10^{24} cm^{-2} and a logarithmic FWHM of 2 dex. This is based on the evidence presented by Alexander et al. (2005) that IRAS 10214's nucleus must be Compton thick ($N_{\rm H} > 1.5 \times 10^{24}$ cm^{-2}). They find that the measured X-ray luminosity is 1–2 dex lower than expected given the measured [O III] line strength and the $L_{\rm [O\,III]}-L_{\rm X}$ correlation (e.g. Netzer et al. 2006). If the obscuring gas column density is significantly larger than $N_{\rm H}$ ∼10^{25} cm^{-2}, then our assumption breaks down and the bolometric luminosity derived here is likely to be too low. However, if one assumes that the X-ray luminosity is dominated by the AGN (and not less obscured star formation), then the $L_{\rm O\,III}$ shows that the hydrogen column density cannot be significantly larger than 10^{25} cm^{-2} (Alexander et al. 2005). Note that if the NLR (and hence the [O III] λ5007 flux) has a lower magnification factor than the active nucleus, as predicted by our lens model, this will increase the $L_{\rm [O\,III]}-L_{\rm X}$ discrepancy, yielding greater evidence that the active nucleus is Compton thick.

Under these assumptions, we find $\log(N_{\rm H}) = 23.5\pm^{0.4}_{0.2}$ cm^{-2}, from the MCMC spectral fit illustrated in Fig. 7. By comparison with the model type I X-ray spectrum, we can estimate the intrinsic X-ray luminosity of IRAS 10214 and therefore the intrinsic bolometric luminosity. We find $L_{\rm bol,X-ray} = 1.3\pm^{1.2}_{0.7} \times 10^{39}\,\mu_{\rm X}^{-1}$ W ($3.4 \times 10^{12}\,\mu_{\rm X}^{-1}$ L$_\odot$), where $\mu_{\rm X}$ is the magnification of the X-rays emanating from the AGN core. We do not have a strong constraint on the magnification of this unresolved X-ray detection given its low S/N and the absolute astrometric accuracy of *Chandra* ($3\sigma = 0.8$ arcsec);[3] however, as an indicative estimate, we assume that $\mu_{\rm X} = \mu_{\rm EVN}$, which yields an intrinsic bolometric estimate $L_{\rm bol,X-ray} = 5.3\pm^{5.1}_{3.0} \times 10^{10}$ L$_\odot$. We emphasize that this X-ray magnification could vary substantially from the assumed magnification since microlensing is observed in X-ray emitting regions of AGN (e.g. Pooley et al. 2007; Chen et al. 2012), but not frequently in the radio emitting regions (e.g. Koopmans et al. 2003), suggesting that the former are constrained to smaller regions than the latter. However, co-spatial regions smaller than the VLBI core will tend to a magnification of $\mu_{\rm X} \sim \mu_{\rm EVN} \sim 68$.

The 20–30 ks observations here combined with the magnification ($\mu \sim 68$) make this almost equivalent to the most sensitive X-ray field ever observed (*Chandra Deep Field*-South, 4 Ms); however, the lack of spectral resolution results in large degeneracies (particularly due to the scattering fraction) which are overcome to some extent with our assumed priors. Further progress will only be achieved with greater depth and spectral coverage/resolution.

7.5 Bolometric luminosity of IRAS 10214

In Fig. 8 we show the 2D posterior PDF of the X-ray derived hydrogen column density ($N_{\rm H}$) and bolometric luminosity, which illustrates the degeneracy between these two parameters (below the Compton limit). Overplotted are two dashed red lines that indicate the two dust bolometric luminosity estimates. The blue horizontal line and shading indicate the $L_{\rm bol,O\,III}$ estimate along with its 68 per cent confidence levels. Finally, the green dashed line shows the estimate based on the scattered quasar light. While the uncertainty is large in all of the above methods (∼0.3−0.5 dex), they

[3] http://cxc.harvard.edu/cal/ASPECT/celmon/

all show a reasonably consistent picture of a hidden quasar with intermediate luminosity. Furthermore, our highest estimate is that which we expect to be most contaminated by star formation (i.e. the 210 K dust bolometric luminosity estimate).

The five methods here are based on high-exposure space telescope observations and so it is challenging to see where we will make substantial progress in determining the bolometric luminosity of obscured quasars like IRAS 10214 before the next generation of telescopes or extended, dedicated programmes with current facilities. We adopt a quasar bolometric luminosity that is the weighted mean of the five methods presented here, which results in a value of $\log_{10}(\langle L_{\rm bol,\,QSO}\rangle/{\rm L}_{\odot}) = 11.34 \pm 0.27$; however, we stress the myriad systematic uncertainties associated with each method.

8 BLACK HOLE PARAMETERS

8.1 Black hole mass

As discussed in Section 1 and D13a, Goodrich et al. (1996) found IRAS 10214 to have polarized broad emission lines (C III, C IV, Lyα/N V) with Keck spectropolarimetry. In the standard quasar unification model (Antonucci 1993), this is consistent with a dusty toroidal structure obscuring a direct view of the AGN core and its associated BLR. However, a fraction of the BLR emission is scattered off dust and electrons into the observer's line of sight. This polarizes the radiation providing a very useful tool in the dissection of AGN. Dust of course reddens the scattered radiation, whereas electrons do not alter the spectrum of the incident radiation with any wavelength dependence. Discerning the nature of the scatterers is possible in principle, however not at present in the case of IRAS 10214 due to the low-S/N polarized spectrum.

Goodrich et al. (1996) measured a polarized C IV line width of $\Delta v_{\rm C\,IV} \sim 6000\,{\rm km\,s^{-1}}$. Following the Vestergaard & Peterson (2006) calibration, the black hole mass can be estimated from the C IV velocity width via

$$\log\left(M_{\rm BH}({\rm C\,IV})\right) = \log\left(\left[\frac{\Delta V_{\rm C\,IV}}{1000\,{\rm km\,s^{-1}}}\right]^2 \left[\frac{\lambda L_{\lambda}(1350\,{\rm \AA})}{10^{44}\,{\rm erg\,s^{-1}}}\right]^{0.53}\right) + (6.66 \pm 0.01). \quad (3)$$

We determine the value $\nu L_{1350} = 7.3 \times 10^{37}$ W based on the quasar bolometric luminosity derived in Section 7 and an average quasar spectrum (Elvis et al. 1994). This yields a black hole mass of $\log_{10}(M_{\rm BH}/{\rm M}_{\odot}) = 8.36 \pm 0.56$. Even with this large uncertainty, this places the black hole mass two orders of magnitude above the 'knee' (M^* value) of the $z = 0$ black hole mass function; however, it is certainly not amongst the most massive black holes ($>10^9\,{\rm M}_{\odot}$) observed at this epoch and earlier (e.g. Kurk et al. 2007). Based on this black hole mass and the mean quasar bolometric luminosity derived in Section 7, we can estimate the Eddington ratio

$$\begin{aligned}\eta &= \langle L_{\rm bol,QSO}\rangle/L_{\rm Edd}\\ &= 2.2 \times 10^{11}\,{\rm L}_{\odot}/7.4 \times 10^{12}\,{\rm L}_{\odot}\\ &= 3^{+7}_{-2}\ \text{per cent}. \end{aligned} \quad (4)$$

This indicates (even with the large uncertainty) that the accretion rate is likely to be below the typical 10 per cent level for actively accreting, radio-loud quasars, consistent with the low intrinsic radio core flux ($S_{1.7\,\rm GHz} \sim 3\,\mu$Jy).

While there is some contention regarding the validity of the C IV FWHM as a black hole mass estimator (e.g. Baskin & Laor 2005; Shen et al. 2008; Croom 2011), the polarized C IV line is perhaps the most robust black hole mass estimator we have at our disposal for this obscured quasar. We emphasize the large uncertainty of 0.56 dex as well as the caution raised by Baskin & Laor (2005) regarding the use of the C IV FWHM in black hole mass estimates. Included in this uncertainty is the inclination dependency, since the BLR has been shown to be more disc-like rather than spherical (see a discussion in Jarvis & McLure 2002, 2006, and references therein). This is the first estimate of the black hole mass in IRAS 10214.

As a consistency check, we estimate the black hole mass, using a second, significantly less secure method based on the rest-frame 5 GHz luminosity and Eddington rate ($L/L_{\rm Edd}$; Lacy et al. 2001), based on their derived correlation between the black hole mass and radio luminosity in the analysis of 60 quasars selected from the FIRST[4] Bright Quasar Survey (FBQS; Gregg et al. 1996; White et al. 2000). Their correlation is re-arranged as follows:

$$\log_{10}(M_{\rm BH}) = \frac{\log_{10}(L_{5\,\rm GHz}) - 1.0\,\log_{10}(L/L_{\rm Edd}) - 7.9}{1.9}, \quad (5)$$

where $M_{\rm BH}$ is in units of ${\rm M}_{\odot}$ and $L_{5\,\rm GHz}$ is in units of W Hz^{-1} sr^{-1}. The scatter in this relation is very large (1.1 dex), since a number of important physical effects are neglected such as black hole spin and Doppler brightening (Jarvis & McLure 2002). Nonetheless, equation (5) does provide an indicative black hole mass, which we calculate assuming the EVN 1.66 GHz (rest-frame 5.5 GHz) flux density of $S_{\rm int} = 220 \pm 37\,\mu$Jy, its derived magnification of $\mu_{EVN} = 68$, and accretion rates of $L/L_{\rm Edd} = 1$, 10 and 100 per cent. This results in black hole estimates of $\log_{10}(M_{\rm BH,5\,GHz}/{\rm M}_{\odot}) = 8.79$, 8.27 and 7.74 ± 1.1 for accretion efficiencies of $L/L_{\rm Edd} = 1$, 10 and 100 per cent, respectively. The reasonable agreement is encouraging; however, we use the C IV FWHM estimate for the remainder of the paper since this method is significantly more robust.

8.2 Black hole–spheroid mass ratio

Based on the black hole mass estimate in Section 8.1, we now constrain the intrinsic stellar mass in IRAS 10214 in order to estimate the black hole to stellar mass ratio. We do not attempt a bulge-to-'disc' decomposition, since this requires detailed two-dimensional Sérsic fitting of the source-plane inversion of a (preferably) pixel-based lensing inversion algorithm which is beyond the scope of this paper. We therefore make the assumption that the bulge mass dominates over the host stellar mass. The tentative 4000 Å break in Lacy et al. (1998) suggests that an older stellar population, more likely to be concentrated in a bulge, may dominate the rest-frame optical spectrum. The source-plane scale radius of the *HST F160W* component in Deane et al. (in preparation) is $r_{\rm s} \sim 500$ pc which is significantly smaller than the CO (1→0) source-plane scale radius ($r_{\rm CO} = 5.7$ kpc) derived in D13b. This is consistent with the expectation that a bulge component will have a radius significantly smaller than the extended gas reservoir. Finally, we assume that the stellar mass dominates the *total* mass inside this loosely defined spheroid which is consistent with strong gravitational lensing results coupled with central lens stellar velocity dispersion measurements (Treu & Koopmans 2004; Koopmans et al. 2009). The latter provide constraints on the slope of the total potential which when combined with the light distribution allow measurements of the stellar to total mass ratio at the bulge effective radius.

[4] Faint Images of the Radio Sky at Twenty-cm, http://sundog.stsci.edu

We select the *HST F*160*W* map to estimate the total magnification since it has a significantly higher S/N than any of the other filters that are dominated by stellar emission. We derive a magnification of $\mu_{\rm stellar} = 14.1\pm^{1.6}_{1.2}$ (Deane et al., in preparation); however, we re-emphasize the associated systematic uncertainty described in D13a which is in the range of 20–40 per cent. The *HST F*160*W* lensing inversion is part of a detailed lensing analysis of several *HST* filters which is beyond the scope of this paper.

Spectrally derived stellar mass estimates are challenging in the case of IRAS 10214 since the emission is AGN dominated in the near-UV and the near-IR with an ill-defined transition into the stellar dominance at optical wavelengths, suggested by the tentative Balmer break. Ideally, we would make a mass estimate in the NIR; however, in addition to the AGN emission, the lens galaxy makes a substantial, yet unconstrained contribution at this wavelength (Verma et al., in preparation). A compromise is to make a coarse estimate from a single filter that we believe is dominated by stellar continuum emission.

We adopt the *HST F*212*N* magnitude of $m_{F212N} = 19.63 \pm 0.34$ determined by Simpson et al. (in preparation) since this wavelength is a less biased tracer of stellar mass and it is the only *HST* filter free of line contamination (Simpson et al., in preparation). The main difference between this and the *HST F*160*W* map is likely to be dust extinction (between rest-frame 490 and 650 nm) and therefore does not result in a substantially different solid angle (and hence the resulting magnification) between these two filters. We compare this apparent magnitude with the range of *K*-corrected *HST F*212*N* apparent magnitudes derived from a wide range of star formation histories (SFH) using the models of Bruzual & Charlot (2003). We vary the formation redshift in the range $z_{\rm f} = 6$–10 and metallicity within $Z = 0.008$–0.05; SFH models include SSP, singular burst and exponential, where the latter have τ values in the range 0.1–5 Gyr. Assuming the *HST F*160*W* magnification $\mu_{F160W} = 14.1\pm^{1.6}_{1.2}$, this results in a range of predicted stellar masses of $\log(M^*(z = 2.3)/{\rm M}_\odot) = 9.6$–$10.6$ and a mean of $\langle\log(M^*(z = 2.3)/{\rm M}_\odot)\rangle = 10.1 \pm 0.5$, where the uncertainties are conservatively assumed to be half the full range.

Our dynamical and gas mass estimates in D13b imply a stellar mass of $M_{\rm stellar,\,dyn} = 6.8 \pm 1.7 \times 10^9\,{\rm M}_\odot$ which is calculated by assuming the mean gas fraction for a large sample of IR luminous galaxies (Bothwell et al. 2013) and a dark matter fraction within the CO (1→0) effective radius (Daddi et al. 2010). The D13b stellar mass is in good agreement with our *HST F*212*N* estimate. The stated assumptions, along with this rough stellar mass of $\langle\log(M^*(z = 2.23)/{\rm M}_\odot)\rangle = 10.1 \pm 0.5$, enable an estimate of the central supermassive black hole to spheroid mass ratio, $M_{\rm BH}/M_{\rm spheroid} = 0.02$, admittedly with large uncertainty (∼0.8 dex). However, this is ∼1.2 dex larger than the typical ratio found at $z \simeq 0$; however, both are consistent with the suggested evolution of this relation for AGN host galaxies. For example, assuming $\alpha \sim 2 \pm 1$ (where $\alpha \propto M_{\rm BH}/M_{\rm spheroid}$), we expect an increase in the $M_{\rm BH}/M_{\rm spheroid}$ relation by a factor of $11\pm^{25}_{8}$ at a redshift of $z = 2.3$, in agreement with our derived values.

The black hole to spheroid mass ratio is typically $M_{\rm BH}/M_{\rm spheroid}$ ∼0.1–0.2 per cent at $z \sim 0$ (e.g. Merritt & Ferrarese 2001; Marconi & Hunt 2003; Häring & Rix 2004), but, as stated above, is found to increase for high-redshift quasars, albeit with large uncertainty and selection effects, by a number of authors (e.g. McLure et al. 2006; Peng et al. 2006; Treu et al. 2007; Bennert et al. 2011). Peng et al. (2006) investigated a sample of 31 gravitationally lensed and 20 non-lensed AGN and found that the $M_{\rm BH}/M_{\rm bulge}$ mass increased by a factor of $\gtrsim 4\pm^{2}_{1}$ for $z > 1.7$. McLure et al. (2006) performed a similar study with the 3CRR sample (Laing, Riley & Longair 1983), which consisted of 170 radio-loud, low-frequency selected AGN. They found an evolution of $M_{\rm BH}/M_{\rm spheroid} \propto (1+z)^\alpha$, where $\alpha = 2.07 \pm 0.76$. Treu et al. (2007) and Bennert et al. (2011) find consistent values of $\alpha = 1.5 \pm 1.0$ and 1.96 ± 0.55 for samples with mean redshifts of $z \sim 0.36$ and $z \sim 2$, respectively. The former sample was made up of 20 Seyferts, while the latter comprised of 11 X-ray selected, broad-line AGN in a GOODS-N/S sample. There are clearly a number of independent studies that suggest that quasar black hole growth precedes the full development of the stellar component to some degree; however, selection biases could yield similar results, as argued in Lauer et al. (2007).

Although the uncertainties are large, the overall picture strongly supports that the majority of the black hole growth precedes the stellar mass assembly for this obscured quasar (assuming that IRAS 10214 will evolve to be consistent with the local $M_{\rm BH}/M_{\rm spheroid}$ relation). This is contrary to the 'undermassive' black hole masses measured in $z \sim 2$ submillimetre galaxies (SMGs) by Alexander et al. (2008) and Biggs, Younger & Ivison (2010). Alexander et al. (2008) made $M_{\rm BH}$ estimates in six broad-line SMGs using Hβ and Hα line widths using the Greene & Ho (2005) virial estimator, and found that (a) they have black hole masses $\gtrsim$3 times smaller than 'normal' galaxies in the local Universe of comparable mass and (b) have $\gtrsim$10 times smaller black hole masses than that predicted for $z \sim 2$ populations. From their fig. 4, they derive an $M_{\rm BH}/M_{\rm spheroid}$ ratio ≈ 2.5–4×10^{-4} for the CO dynamics and stellar mass determined bulge mass. Biggs et al. (2010) performed a VLBI survey of six SMGs with a mean redshift of $z \sim 2$. They calculate black hole masses (and upper limits) based on the Lacy et al. (2001) $L_{5\,\rm GHz}$ method and their 1.6 GHz VLBI observations of all six SMGs. Although the uncertainty is very large (1.1 dex), all six of their objects have black hole masses (or upper limits) that are ∼0.2–1.3 dex *below* the expected value based on the Häring & Rix (2004) finding that $M_{\rm BH}/M_{\rm spheroid} = 0.0014 \pm 0.0004$ in the local Universe. The mean of their quoted stellar masses and black hole masses (as well as upper limits) implies a $\log(M_{\rm BH}/M_{\rm spheroid}) \approx 0.0002$ with the quoted uncertainty of 1.1 dex.

Despite the large uncertainties, there appears to be one to two orders of magnitude difference between the black hole to spheroid mass ratio in SMGs and that in the obscured quasar IRAS 10214. This tentatively implies very different evolutionary paths for these two object classes, despite their apparent similarities in many parts of the global SED. However, this may be a result of the selection bias outlined in Lauer et al. (2007), particularly since we demonstrate in this work that the AGN is preferentially magnified by an order of magnitude when compared to the spatially resolved JVLA CO (1→0) map in D13b.

Nonetheless, the high $M_{\rm BH}/M_{\rm spheroid}$ ratio, relatively regular CO (1→0) velocity map (D13b), single EVN detection and highly magnified yet uniform *HST F*160*W* morphology are all consistent with IRAS 10214 being an example of a fairly typical AGN host galaxy at $z \sim 2$, as found in Kocevski et al. (2012). These authors present deep *HST F*160*W* (*H*-band) and *HST F*125*W* (*J*-band) observations of 72 intermediate X-ray luminosity ($L_{\rm X} \sim 10^{42}$–$10^{44}\,{\rm erg\,s^{-1}}$) AGN selected from the 4 Ms *Chandra* observation of the *Chandra Deep Field*-South, as part of the CANDELS survey (Grogin et al. 2011). They find that AGN host galaxies at $z \sim 2$ appear no more likely to be part of a major merger than a control sample of galaxies in the same mass range. One caveat, however, is that most major merger traits may be erased by the time the resultant AGN activity begins. The Kocevski et al. (2012) result is consistent with Schawinski et al. (2012), who show that a

sample of $z \sim 2$ highly obscured quasar host galaxies are not major mergers, but have reasonably smooth morphologies with Sérsic indices consistent with discs. Furthermore, Cisternas et al. (2011) and Georgakakis et al. (2009) find consistent results at $z \sim 1$. These results form part of a growing consensus that major mergers do not play the dominant role in triggering intermediate-luminosity AGN activity as outlined in the classical Sanders et al. (1988) scenario, where the merger-induced loss of angular momentum leads to black hole accretion. Moreover, these studies all find that AGN hosts at $z \sim 1{-}3$ are predominantly disc-like in morphology, which is what the CO (1→0) kinematics tentatively suggest for IRAS 10214 (D13b).

This paper (together with the series it is part of) therefore suggests that IRAS 10214 hosts a supermassive black hole that has primarily grown in mass due to secular evolution, minor interactions and/or internal instabilities, rather than the classical major merger-induced scenario. We propose that IRAS 10214 is therefore a relatively typical intermediate-luminosity AGN at $z \sim 2$; however, its active nucleus is preferentially lensed by an order of magnitude with respect to the star-forming disc.

9 CONCLUSIONS

We have performed a deep ($\sigma = 23\,\mu$Jy beam^{-1}), 1.7 GHz EVN observation on IRAS 10214, a lensed $z = 2.3$ obscured quasar with prodigious star formation. The VLBI observation provides a brightness temperature filter which is unobscured by dust and therefore allows us to image the obscured active nucleus with an effective angular resolution of $\lesssim$50 pc at $z = 2.3$, after correcting for gravitational lensing. These EVN observations permit a number of conclusions to be drawn.

(i) The AGN core as traced by the EVN 1.7 GHz detection has a flux density peak of $S_{\rm peak} = 209 \pm 23\,\mu$Jy beam^{-1} which makes up ∼20 per cent of the total 1.7 GHz flux density of a MERLIN map presented in D13a. The EVN detection appears unresolved, with an integrated flux density of $S_{\rm peak} = 220 \pm 37\,\mu$Jy. The remainder of the MERLIN 1.7 GHz flux is likely to be split between star formation and large-scale ($\gtrsim$200 pc) jets.

(ii) The fact that the AGN core is a single detection and is northwards of the *HST F*814*W* arc strongly advocates that the *HST F*814*W* arc is not a triple-image system that is merged by the *HST* PSF. This supports the lens model derived by D13a which suggests that the *HST F*814*W* map is comprised of a single arc and the observed double peak corresponds to an intrinsic structure at the rest-frame UV wavelengths.

(iii) The AGN core is located at a position qualitatively consistent with the spatially resolved polarization properties of the UV map reported in Nguyen et al. (1999). Moreover, it is consistent with their prediction of the active nucleus position based on these polarization properties as well as the narrow-band *HST* observations which suggest that the BLR centre of curvature is northwards of the NLR centre of curvature (Simpson et al., in preparation).

(iv) If the AGN core position and size are well approximated by the radio core detected in this EVN observation, then the AGN is preferentially magnified by over an order of magnitude when compared to a spatially resolved JVLA CO (1→0) map (D13b), where the latter can be used as a star formation proxy. This confirms the effective 'chromaticity' of this strong-lens system (discussed in D13a and D13b), which is caused by different emission regions undergoing different magnification boosts due to their relative size and position with respect to the caustic. This effect may be particularly relevant in the case of far-infrared bright, strongly lensed galaxies discovered by the *Herschel Space Observatory* (Negrello et al. 2010).

(v) The configuration of the EVN core and *HST* UV arc support our previous claim that this is an asymmetric (or one-sided) source where we observe the line-of-sight NLR, whilst the 'counter-NLR' is obscured by a significant host dust reservoir, consistent with examples in the nearby Universe (e.g. Liu & Pooley 1991; Simpson et al. 1997).

(vi) We derive a black hole mass of $\log_{10}(M_{\rm BH}/{\rm M}_\odot) = 8.36 \pm 0.56$ and a bolometric luminosity of $\log_{10}(\langle L_{\rm bol,\,QSO}\rangle/{\rm L}_\odot) = 11.34 \pm 0.27$ dex, which suggests a low accretion rate of $\eta \sim 3\pm^{7}_{2}$ per cent, albeit with significant uncertainty.

(vii) Our crudely derived black hole to spheroid mass ratios are consistent with the suggested evolution of this parameter in AGN host galaxies (McLure et al. 2006; Peng et al. 2006; Treu et al. 2007; Bennert et al. 2011). The $M_{\rm BH}/M_{\rm spheroid}$ ratio in IRAS 10214 is one to two orders of magnitude larger than that of $z \sim 2$ SMGs based on optical and radio analyses (Alexander et al. 2008; Biggs et al. 2010), providing a tentative suggestion that these two object classes may follow different evolutionary paths (i.e. secular rather than merger-induced black hole growth). However, this picture is sensitive to the large black hole mass uncertainties and selection effects (e.g. Lauer et al. 2007).

These results point towards an intermediate-luminosity AGN; however, our X-ray modelling find it to be a highly obscured nucleus. The mean hydrogen column density $\overline{N_{\rm H}} \sim 10^{23.5}\,{\rm cm}^{-2}$ explains the excessive [O III] λ5007 luminosity in comparison with the derived X-ray luminosity (Alexander et al. 2008). This X-ray modelling predicts a strong Fe K line to be observed if the required sensitivity is achieved. The unobscured, intrinsic quasar bolometric luminosity ($2.2 \times 10^{11}\,{\rm L}_\odot$) is well supported with independent bolometric luminosity estimates and suggests inefficient, sub-Eddington accretion on to the central black hole which is consistent with the low intrinsic radio core flux ($S_{1.7\,{\rm GHz}} \sim 3\,\mu$Jy). Comparison with a large sample of AGN host galaxies at $z \sim 1.5$–2.5 (Kocevski et al. 2012) suggests that IRAS 10214 is plausibly a fairly typical AGN host based on the lack of major merger traits and the relatively regular CO (1→0) velocity map, consistent with a disc-like morphology. Therefore, the key difference in the case of IRAS 10214 may be that it has a preferentially magnified active nucleus. This case study is not only a clear demonstration of the significant SED distortion due to preferential lensing, but also a preview of what can be achieved with the enhanced sensitivity and new wide-field capabilities of the VLBA as well as the EVN which will detect large samples of low-luminosity AGN ($L_{5\,{\rm GHz}} \lesssim 10^{22}$ W Hz^{-1} sr^{-1}) over well-studied multiwavelength fields (e.g. Middelberg et al. 2011). These surveys will play an important role in characterizing AGN activity over cosmic time, particularly for the obscured AGN population.

ACKNOWLEDGEMENTS

This paper, as well as the series it forms a part of, is dedicated to the memory of Steve Rawlings. We are grateful to the EVN chair for awarding discretionary telescope time to perform a calibrator search in the vicinity of the target source – this was key to the success of the observation of IRAS 10214. We thank Zsolt Paragi who generously provided technical expertise in the planning and execution of the EVN observations. We thank the anonymous referee for the level

of scrutiny applied to the paper which made a number of important improvements to the work. The European VLBI Network is a joint facility of European, Chinese, South African and other radio astronomy institutes funded by their national research councils. The National Radio Astronomy Observatory is a facility of the National Science Foundation operated under cooperative agreement by Associated Universities, Inc. This work made use of the Swinburne University of Technology software correlator, developed as part of the Australian Major National Research Facilities Programme and operated under licence. This effort/activity was supported by the European Community Framework Programmes 6 and 7, Square Kilometre Array Design Studies (SKADS), contract no. 011938 and PrepSKA, grant agreement no.: 212243. RPD gratefully acknowledges funding that enabled visits to JIVE which were supported by the European Community Framework Programme 7, Advanced Radio Astronomy in Europe, grant agreement no.: 227290. PJM acknowledges support from the Royal Society in the form of a University Research Fellowship.

REFERENCES

Alexander D. M., Chartas G., Bauer F. E., Brandt W. N., Simpson C., Vignali C., 2005, MNRAS, 357, L16
Alexander D. M. et al., 2008, AJ, 135, 1968
Antonucci R., 1993, ARA&A, 31, 473
Ao Y., Weiß A., Downes D., Walter F., Henkel C., Menten K. M., 2008, A&A, 491, 747
Baskin A., Laor A., 2005, MNRAS, 356, 1029
Bennert V. N., Auger M. W., Treu T., Woo J.-H., Malkan M. A., 2011, ApJ, 742, 107
Biggs A. D., Younger J. D., Ivison R. J., 2010, MNRAS, 408, 342
Blandford R. D., Kochanek C. S., Kovner I., Narayan R., 1989, Sci, 245, 824
Bothwell M. S. et al., 2013, MNRAS, 429, 3047
Bruzual G., Charlot S., 2003, MNRAS, 344, 1000
Chen B., Dai X., Kochanek C. S., Chartas G., Blackburne J. A., Morgan C. W., 2012, ApJ, 755, 24
Cisternas M. et al., 2011, ApJ, 726, 57
Condon J. J., 1997, PASP, 109, 166
Croom S. M., 2011, ApJ, 736, 161
Daddi E. et al., 2010, ApJ, 713, 686
Deane R. P. et al., 2013a, MNRAS, 430, 2 (D13a)
Deane R. P. et al., 2013b, MNRAS, submitted (D13b)
Downes D., Solomon P. M., 1998, ApJ, 507, 615
Dunlop J. S., Peacock J. A., 1990, MNRAS, 247, 19
Dyer C. C., Shaver E. G., 1992, ApJ, 390, L5
Eales S. et al., 2010, PASP, 122, 499
Efstathiou A., 2006, MNRAS, 371, L70
Eisenhardt P. R., Armus L., Hogg D. W., Soifer B. T., Neugebauer G., Werner M. W., 1996, ApJ, 461, 72
Elmegreen B. G., 1999, ApJ, 517, 103
Elston R., McCarthy P. J., Eisenhardt P., Dickinson M., Spinrad H., Januzzi B. T., Maloney P., 1994, AJ, 107, 910
Elvis M. et al., 1994, ApJS, 95, 1
Evans A. S., Scoville N. Z., Dinshaw N., Armus L., Soifer B. T., Neugebauer G., Rieke M., 1999, ApJ, 518, 145
Fabian A. C., Cutri R. M., Smith H. E., Crawford C. S., Brandt W. N., 1996, MNRAS, 283, L95
Ferrarese L., Merritt D., 2000, ApJ, 539, L9
Fiore F. et al., 2008, ApJ, 672, 94
Gebhardt K. et al., 2000, ApJ, 539, L13
Georgakakis A. et al., 2009, MNRAS, 397, 623
Gilli R., Comastri A., Hasinger G., 2007, A&A, 463, 79
Goodrich R. W., Miller J. S., Martel A., Cohen M. H., Tran H. D., Ogle P. M., Vermeulen R. C., 1996, ApJ, 456, L9
Greene J. E., Ho L. C., 2005, ApJ, 630, 122
Gregg M. D., Becker R. H., White R. L., Helfand D. J., McMahon R. G., Hook I. M., 1996, AJ, 112, 407
Grogin N. A. et al., 2011, ApJS, 197, 35
Häring N., Rix H.-W., 2004, ApJ, 604, L89
Helmboldt J. F. et al., 2007, ApJ, 658, 203
Iwasawa K., Vignali C., Evans A. S., Sanders D. B., Trentham N., 2009, New Astron., 15, 58
Jarvis M. J., McLure R. J., 2002, MNRAS, 336, L38
Jarvis M. J., McLure R. J., 2006, MNRAS, 369, 182
Keeton C. R., Gaudi B. S., Petters A. O., 2003, ApJ, 598, 138
Kettenis M., van Langevelde H. J., Reynolds C., Cotton B., 2006, in Gabriel C., Arviset C., Ponz D., Solano E., eds, ASP Conf. Ser. Vol. 351, Astronomical Data Analysis Software and Systems XV. Astron. Soc. Pac., San Francisco, p. 497
Klöckner H.-R., Martínez-Sansigre A., Rawlings S., Garrett M. A., 2009, MNRAS, 398, 176
Kocevski D. D. et al., 2012, ApJ, 744, 148
Koopmans L. V. E. et al., 2003, ApJ, 595, 712
Koopmans L. V. E. et al., 2009, ApJ, 703, L51
Kurk J. D. et al., 2007, ApJ, 669, 32
Lacy M., Rawlings S., Serjeant S., 1998, MNRAS, 299, 1220
Lacy M., Laurent-Muehleisen S. A., Ridgway S. E., Becker R. H., White R. L., 2001, ApJ, 551, L17
Laing R. A., Riley J. M., Longair M. S., 1983, MNRAS, 204, 151
Lauer T. R., Tremaine S., Richstone D., Faber S. M., 2007, ApJ, 670, 249
Lawrence A. et al., 1993, MNRAS, 260, 28
Liu R., Pooley G., 1991, MNRAS, 253, 669
Madau P., Ghisellini G., Fabian A. C., 1994, MNRAS, 270, L17
Madau P., Ferguson H. C., Dickinson M. E., Giavalisco M., Steidel C. C., Fruchter A., 1996, MNRAS, 283, 1388
Magorrian J. et al., 1998, AJ, 115, 2285
Marconi A., Hunt L. K., 2003, ApJ, 589, L21
Martínez-Sansigre A., Rawlings S., Lacy M., Fadda D., Marleau F. R., Simpson C., Willott C. J., Jarvis M. J., 2005, Nat, 436, 666
McKean J. P. et al., 2007, MNRAS, 378, 109
McLure R. J., Jarvis M. J., Targett T. A., Dunlop J. S., Best P. N., 2006, MNRAS, 368, 1395
Merritt D., Ferrarese L., 2001, MNRAS, 320, L30
Middelberg E. et al., 2011, A&A, 526, A74
Miller P., Rawlings S., Saunders R., Eales S., 1992, MNRAS, 254, 93
Mor R., Netzer H., Elitzur M., 2009, ApJ, 705, 298
More A., McKean J. P., More S., Porcas R. W., Koopmans L. V. E., Garrett M. A., 2009, MNRAS, 394, 174
Muxlow T. W. B., Pedlar A., Wilkinson P. N., Axon D. J., Sanders E. M., de Bruyn A. G., 1994, MNRAS, 266, 455
Negrello M. et al., 2010, Sci, 330, 800
Netzer H., Mainieri V., Rosati P., Trakhtenbrot B., 2006, A&A, 453, 525
Nguyen H. T., Eisenhardt P. R., Werner M. W., Goodrich R., Hogg D. W., Armus L., Soifer B. T., Neugebauer G., 1999, AJ, 117, 671
Pei Y. C., 1992, ApJ, 395, 130
Peng C. Y., Impey C. D., Rix H.-W., Kochanek C. S., Keeton C. R., Falco E. E., Lehár J., McLeod B. A., 2006, ApJ, 649, 616
Polletta M. d. C. et al., 2006, ApJ, 642, 673
Pooley D., Blackburne J. A., Rappaport S., Schechter P. L., 2007, ApJ, 661, 19
Rowan-Robinson M. et al., 1991, Nat, 351, 719
Rowan-Robinson M. et al., 1993, MNRAS, 261, 513
Sanders D. B., Soifer B. T., Elias J. H., Madore B. F., Matthews K., Neugebauer G., Scoville N. Z., 1988, ApJ, 325, 74
Schawinski K., Simmons B. D., Urry C. M., Treister E., Glikman E., 2012, MNRAS, L488
Schweitzer M. et al., 2007, in Ho L. C., Wang J.-M., eds, ASP Conf. Ser. Vol. 373, The Central Engine of Active Galactic Nuclei. Astron. Soc. Pac., San Francisco, p. 501
Scoville N. Z., Yun M. S., Bryant P. M., 1997, ApJ, 484, 702
Serjeant S., Rawlings S., Lacy M., McMahon R. G., Lawrence A., Rowan-Robinson M., Mountain M., 1998, MNRAS, 298, 321

Shen Y., Greene J. E., Strauss M. A., Richards G. T., Schneider D. P., 2008, ApJ, 680, 169
Shi Y. et al., 2006, ApJ, 653, 127
Simpson C., Wilson A. S., Bower G., Heckman T. M., Krolik J. H., Miley G. K., 1997, ApJ, 474, 121
Soifer B. T., Cohen J. G., Armus L., Matthews K., Neugebauer G., Oke J. B., 1995, ApJ, 443, L65
Spergel D. N. et al., 2007, ApJS, 170, 377
Sturm E., Hasinger G., Lehmann I., Mainieri V., Genzel R., Lehnert M. D., Lutz D., Tacconi L. J., 2006, ApJ, 642, 81
Teplitz H. I. et al., 2006, ApJ, 638, L1
Thompson T. A., Quataert E., Murray N., 2005, ApJ, 630, 167
Treu T., Koopmans L. V. E., 2004, ApJ, 611, 739
Treu T., Woo J.-H., Malkan M. A., Blandford R. D., 2007, ApJ, 667, 117
Tristram K. R. W., Schartmann M., 2011, A&A, 531, A99
Tristram K. R. W. et al., 2009, A&A, 502, 67
Vestergaard M., Peterson B. M., 2006, ApJ, 641, 689
White R. L. et al., 2000, ApJS, 126, 133
Wilman R. J., Fabian A. C., 1999, MNRAS, 309, 862
Wilman R. J., Fabian A. C., Cutri R. M., Crawford C. S., Brandt W. N., 1998, MNRAS, 300, L7

This paper has been typeset from a TEX/LATEX file prepared by the author.